Applied Ocean Research 176 (2026) 105288

Contents lists available at ScienceDirect

Applied Ocean Research

journal homepage: www.elsevier.com/locate/apor

Research paper

A parametric Morison-inspired model for wave-induced torque fluctuations on a vertical axis tidal turbine

Y. Saouli [a,b], B. Gaurier [a], G. Germain [a,*], G. Maurice [b]

[a] Ifremer, RDT Research and Technological Development, F-62200 Boulogne-sur-Mer, France
[b] Hydroquest SAS, Meylan, France

ARTICLE INFO

Keywords:
Modelling
Tidal turbine
Vertical axis
Waves
Morison
Torque

ABSTRACT

This paper investigates the effect of surface waves on the hydrodynamic torque fluctuations of vertical axis tidal turbines. Wave-induced orbital velocities and accelerations are shown to generate periodic variations of the incoming flow, leading to significant unsteady torque loads. A reduced-order torque model inspired by Morison-type formulations is here developed to study wave-induced effects on vertical axis tidal turbines. The model is derived and expressed in terms of the instantaneous wave-modified tip-speed ratio and decomposes the torque response into three main parameters: a mean shift term, a linear sensitivity coefficient linking torque fluctuations to tip-speed ratio variations and an inertial coefficient proportional to the orbital acceleration. Phase-averaged analysis reveals the relative importance of velocity-driven and acceleration-driven mechanisms and the wave-induced torque variability is interpreted as a structured perturbation of the stationary performance curve. The results obtained under irregular waves demonstrate that the proposed Morison-type model is able to reproduce the wave-induced contribution to torque fluctuations with a limited number of parameters identified in monochromatic waves. The use of conservative coefficients derived from monochromatic wave tests appears as a promising strategy to bound torque fluctuations under a given sea state. Such an approach would provide a compact and operational modelling framework, positioned between purely linear spectral transfer-function methods and computationally intensive fully unsteady numerical models. This model offers practical perspectives for structural load assessment, performance optimisation and the development of control strategies for VATT operating in wave-exposed sites.

1. Introduction

The large-scale deployment of tidal turbines for renewable energy production relies on a comprehensive understanding of their behaviour under realistic and unsteady marine conditions. Among the various turbine concepts, Vertical Axis Tidal Turbines (VATTs) offer several advantages in complex flow environments (Jaquier, 2011), particularly in shallow water sites where the flow is subject to significant spatio-temporal variations. In contrast to Horizontal Axis Tidal Turbines (HATTs), VATTs are less sensitive to flow directionality and do not require active yaw control, which makes them particularly suitable for highly unsteady or multidirectional inflows. However, VATT configurations also present drawbacks compared to HATT devices, including generally lower peak efficiency in steady uniform flows, more complex unsteady blade loading due to cyclic angle of attack variations. A potentially higher fatigue loading also rises from the undergone periodic torque fluctuations (Nachtane et al., 2020). Despite these limitations, their robustness to flow misalignment and their compact vertical footprint make them attractive for deployment in constrained or environmentally complex marine sites.

In coastal environments such as the Alderney Race, the interaction between surface waves and tidal currents becomes a major factor influencing turbine performance (Guillou et al., 2021). This interaction is especially critical in high-energy tidal sites open to the sea, where surface gravity waves induce unsteady flow components superimposed on the tidal current. Understanding these interactions is therefore crucial for optimising energy production while ensuring the structural reliability and sufficient lifespan of tidal turbines.

Accurately reproducing and characterising wave conditions in laboratory environments is essential for replicating realistic marine settings. Modern approaches to wave modelling, such as those reviewed by Chawla et al. (2021), extend beyond classical Airy wave theory by incorporating nonlinear effects and spectral representations. This provides a more comprehensive state for simulating ocean waves, particularly in intermediate water depths. Indeed, validation of key

* Corresponding author.
E-mail addresses: yanis.saouli@ifremer.fr (Y. Saouli), gregory.germain@ifremer.fr (G. Germain).

https://doi.org/10.1016/j.apor.2026.105288
Received 30 March 2026; Received in revised form 4 September 2026; Accepted 30 September 2026
Available online 12 October 2026
0141-1187/© 2026 The Authors. Published by Elsevier Ltd. This is an open access article under the CC BY license (http://creativecommons.org/licenses/by/4.0/).

Nomenclature

η	Free surface elevation [m]
λ	Wavelength [m]
ν	Water kinematic viscosity [m^2/s]
ω	Set rotational speed [rad/s]
ω_ϕ	Wave pulsation [rad/s]
ω_{eff}	Effective wave pulsation [rad/s]
ρ	Water density
$\sigma()$	standard deviation
C_P	Power coefficient
C_Q	Torque coefficient
C_{Q0}, C_{Q1}, C_{MQ}	Coefficients of the Morison-like modelling
D_e	Equivalent diameter [m]
f_ω	Rotation frequency [Hz]
f_e	Sampling frequency [Hz]
F_r	Froude number [-]
f_{wave}	Wave frequency [Hz]
g	Standard acceleration of gravity [m/s^2]
h	Water depth [m]
H_b	Rotor height [m]
H_m	Model height [m]
h_m	Turbine height [m]
k	Wave number [m^{-1}]
KC	Keulegan–Carpenter number [-]
N_T	Number of wave cycles
P	Power of the rotor column [W]
Q	Torque of the rotor column [N m]
Q_{wave}	Wave-related torque [N m]
R	Rotor radius [m]
R_e	Reynolds number [-]
$S_{ref} = h_m \times w_m$	Reference surface, projected capture area of the turbine [m^2]
T	Wave period [s]
TI_0	Turbulence intensity of the incoming flow [%]
TI_{3D}	3D turbulence intensity of the flow (with the wavemaker) [%]
TSR	Tip Speed Ratio [-]
TSR_{wave}	Phased wave-related TSR [-]
U, V, W	3D velocity components in the (x,y,z) space [m/s]
U_0	Streamwise flow velocity in (0x) [m/s]
u_w	Longitudinal orbital velocity [m/s]
U_{wave}	Wave-related velocity [m/s]
u_i'	Velocity fluctuation component [m/s]
u_w/U_0	Orbital velocity ratio [%]
V_0, W_0	Lateral and vertical incident flow components in (0y) and (0z) [m/s]
V_{part}	LDV measurement volume [mm^3]
V_{ref}	Reference volume of the turbine [m^3]
w_m	Model width [m]
w_w	Vertical orbital velocity [m/s]
(x,y,z)	Tank coordinate system, x the main flow direction
FI()	Fluctuation Intensity
HAT	Horizontal Axis Turbine
LDV	Laser Doppler Velocimetry
PIV	Particle Image Velocimetry
PSD	Power Spectral Density
VAT	Vertical Axis Turbine

wave parameters, such as frequency, wavelength and surface elevation, is critical when scaling controlled environment results to full-scale applications (Vicinanza et al., 2019). In the case of the English Channel, Mackay et al. (2022) showed that the amplitude-period joint distribution must be related to the local current velocity in order to correctly evaluate the loading.

Previous research on Horizontal Axis Tidal Turbines (HATTs) has shown that wave-induced flow fluctuations can lead to significant flow velocity variations, which directly affect power output, mechanical loading and fatigue damage (Huang et al., 2024). In the presence of waves, the local inflow velocity experienced by the turbine can be interpreted as the superposition of two potentials: the mean current velocity and the orbital motion induced by surface waves. These periodic velocity and acceleration fluctuations modify the instantaneous relative flow velocity and tip-speed ratio experienced by the blades depending on the system control, which leads to unsteady hydrodynamic loads, torque oscillations and fatigue-related effects. Recent experimental studies, like those carried out by Zanforlin et al. (2020) and Wang et al. (2021), have investigated the influence of surface waves on turbine loading and wake dynamics. In the same way, numerical studies such as (Arcos et al., 2025) provide insights into the need to account for inertial effect when investigating turbine loads. Their results confirm that wave–current interactions introduce non negligible periodic loading on the rotor and downstream flow, emphasising the need for refined turbine control strategies and performance modelling in wave-influenced environments.

In addition to average methods, time domain approaches offer a complementary framework by preserving the temporal structure of wave-induced fluctuations. It enables a phase-resolved description of the turbine response, which is especially relevant under monochromatic or narrowband wave loading. One such method relies on the Morison formulation (Morison et al., 1950), originally developed for offshore structures, which decomposes the hydrodynamic force into inertia (acceleration-driven) and hydrodynamic (velocity-driven) components. Applied to tidal turbines, this formulation provides a simplified and physically interpretable model of unsteady loads variations induced by wave propagation (Schmitt et al., 2016; Henriques et al., 2022). Moreover, recent studies have demonstrated that wave–current interactions can significantly impact the magnitude and phasing of these hydrodynamic loads (Fu et al., 2021). This underlines the need to account for wave effects in realistic and temporal operating conditions. Several classification and technical institutions have extended or adapted Morison-type formulations for application to renewable marine energy systems. These adaptations are specified in the design standards and include adjustments of hydrodynamic coefficients (Bureau Veritas, 2015a). This implies the use of linearisation techniques and time-domain implementation strategies for coupled wave–current environments (Bureau Veritas, 2015b). These models are commonly used in design codes and engineering software for structural assessment and load predictions under unsteady marine conditions. To investigate the impact of surface waves on tidal turbine performance, a previous vertical axis scale model was tested in the Ifremer flume tank at Boulogne-sur-Mer. This model was studied under a wide range of current (Moreau et al., 2023b) and wave–current conditions (Moreau et al., 2023a), demonstrating the significant influence of surface waves on power variability, unsteady loading and wake dynamics on the experimental scale (Linant et al., 2025). These results highlight the need for tools to estimate the effect of waves on the behaviour of tidal turbines.

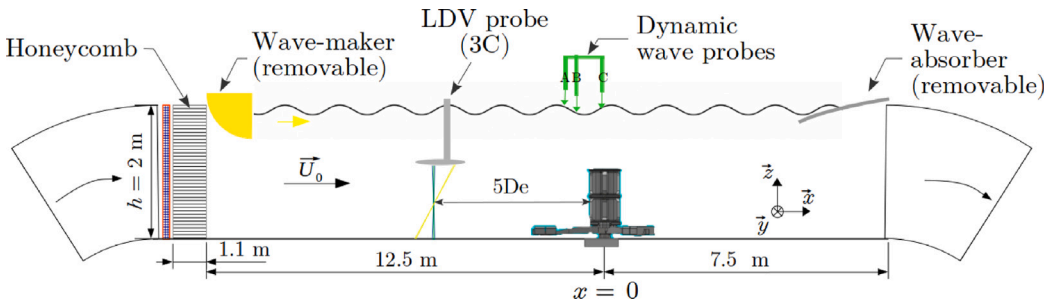


Fig. 1. Schematic description of the flume tank, the turbine location and the instrumentation used (wave probes and laser techniques) during the tests. The wavemaker is here installed at the inlet of the working section, generating waves following the current.

Building on these insights, we worked on the development of a parametric Morison-inspired model for wave-induced torque fluctuations. The present study focuses on a new generation of vertical axis tidal turbines developed by HydroQuest, designed for future deployment at the Flowatt tidal farm site (Raz-Blanchard) (Thiébaut et al., 2018). This work presents an experimental investigation of a 1:20 scale model operating in combined wave–current conditions, with the aim of quantifying the influence of wave parameters on the turbine behaviour and identifying key dynamics to support turbine design and control strategies in wave-exposed environments. The paper first introduces in Section 2 the conditions reproduced in the flume tank and examines the mechanical behaviour of the turbine, including global performance and torque response. In Section 3, a parametric approach is introduced to model the wave-related torque fluctuations. The parameters sets trends are also presented and analysed. A phase-averaged analysis is then conducted to evaluate the periodic nature of wave-induced torque fluctuations. The comparison of the experimental results is done regarding the wave characteristics, based on theoretical wave kinematics and the extended Morison formulation. Prior to the conclusion, the formulation is assessed under irregular sea states to examine whether the reduced set of characteristic coefficients remains sufficient to describe the torque response.

2. Experimental methods and turbine behaviour

2.1. Flume tank disposition and model description

The experimental tests are carried out at the wave and current circulating tank of Ifremer, located in Boulogne-sur-Mer (France). The test section is 18 m long × 4 m wide × 2 m deep (see Fig. 1). The instantaneous flow velocity components are defined as (U, V, W) along the (x, y, z) directions respectively, with x aligned with the main flow propagation direction as displayed in the schematic view. The reference current velocity, denoted as (U_0, V_0, W_0), is measured far upstream of the turbine to avoid the induction zone effect ($5D_e$ upstream from the turbine). The following results are presented for $U_0 \approx [0.6; 0.8]$ m/s and $V_0 = W_0 = 0$ m/s. In the following, the values of U_0 are rounded in the text for ease to reading. The model is placed at the centre of the tank, the x-origin is set to the turbine position, with z = 0 set at the bottom of the tank. The turbine is also centred in the span-wise (Oy) direction of the tank, with $y = 0$ corresponding to the centre of the tank and so of the model.

To ensure low turbulence conditions in current-only tests, a combination of a grid and a honeycomb structure is installed at the inlet of the working section. A turbulence intensity based on the main streamwise velocity component:

$$TI_0 = \frac{\sigma(U)}{\overline{U}} = 1.5\%$$

is reached for the current-only experimental setup, with a boundary layer height of $\delta_{95} \approx 0.250$ m (Ikhennicheu et al., 2019).

To investigate wave-current interaction, a wave-maker and a wave-absorber are used in order to generate waves following or opposing the current, with the wave-maker placed at the inlet or at the outlet of the working section. The wave-absorber is set to reduce wave reflection. It is made of a metallic porous panel (8% porosity) which is fixed at the opposite side of the wave-maker. The wave-maker consists of 8 controllable modules, submerged of 0.50 m from the free surface. The modules follow a pendulum motion to generate waves at the tank surface. The wake generated by the wave-maker (or the damping beach) presence mainly results in the increase of the incoming turbulence intensity TI_{3D} mainly in the upper part of the water column (Gaurier et al., 2025). This facility has been extensively characterised and used for wave–current experiments (Gaurier et al., 2020; Martinez et al., 2021; Allmark et al., 2021; Druault et al., 2026).

Fig. 2 thus presents the actual values of the velocity and turbulence intensity profiles induced by this setup at the turbine location (x,y)=(0,0), for a reference case (wave-maker immersed but inactive) and a case of the wave-maker set at the inlet while generating waves. The profile obtained is considered uniform across the transversal transect (Oy) of the working section. It appears that the mean velocity U_0 and the turbulent intensity TI_{3D} slightly increase from the reference case to the wave propagation case, for both incoming flow conditions of U_0 tested. Based on these observations, it is decided to consider the average flow velocity over the capture area, i.e. the turbine height, as the numerical reference value for each case.

From these assumptions, the instantaneous flow velocity is expressed following the Reynolds decomposition as shown in Eq. (1):

$$U(t) = U_0 + u_w(t) + u'(t) \tag{1}$$

where U_0 denotes the mean current velocity, $u_w(t)$ the orbital velocity component and $u'(t)$ the turbulent part of the flow. To isolate the effect of surface wave kinematics from background turbulence, a wave-related velocity is also defined as:

$$U_{\text{wave}}(t) = U_0 + u_w(t) \tag{2}$$

This definition ensures that the subsequent analysis and modelling of wave-induced fluctuations rely on the orbital velocity contribution, without disturbance from extraneous turbulent aspects.

Measurement tools

The incoming flow velocity is evaluated using a Dantec 3-Component Laser Doppler Velocimeter (LDV-3C) in non-coincident mode, so that each velocity component is measured independently from the others. The probe can be observed in Fig. 3(a). The acquisition time is 3 min per run to guarantee the convergence of mean and standard deviation velocity, as the sampling frequency depends on the number of particles passing through the measurement volume of $V_{part} \approx 0.01$ mm^3. For these measurements, an average sampling frequency of the order of

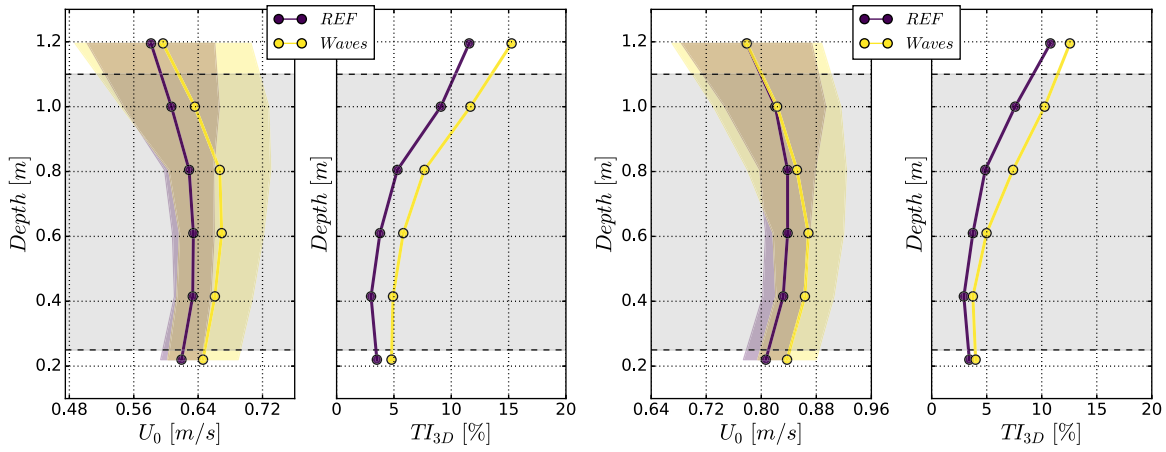


Fig. 2. Horizontal velocity profiles evaluated at the turbine location for the immersed/inactive wavemaker (REF) and the immersed/active wavemaker (Waves). The standard deviation around the mean velocity is represented by the colorised area. The area over which is determined the effective average velocity is represented by the grey surface.

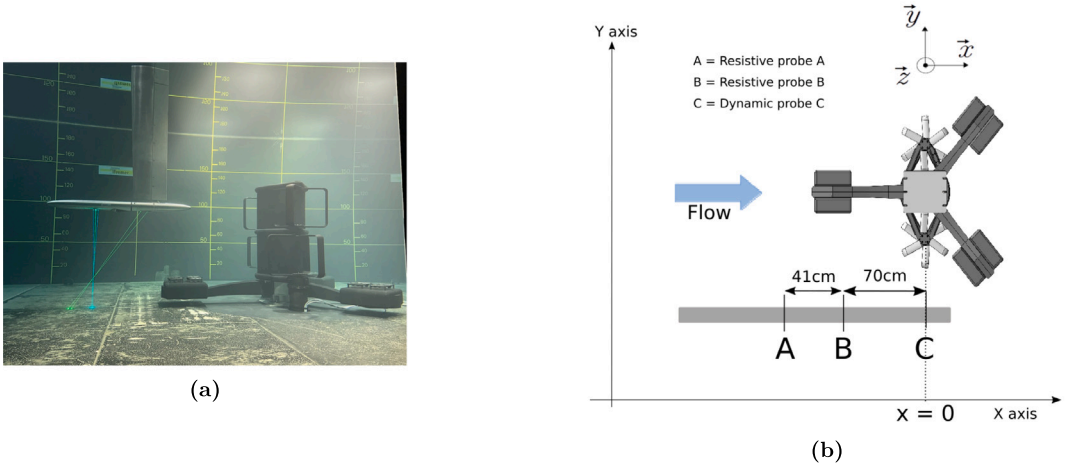


Fig. 3. (a) Photo of the turbine model in the tank and the LDV-3C probe disposed upstream from the turbine. (b) Gauges positions relative to the x-axis turbine position.

90 Hz is obtained. A method of removing the 10th and 90th quantiles is applied in order to avoid detection outliers. Based on the probe orientation and its calibration, an uncertainty of 2% in the time averaged velocity for a flow of 1.00 m/s is estimated for this measurement duration and sampling (e.g. $U_0 = 1.00 \pm 0.02$ m/s).

A set of three wave gauges, including two resistive gauges and one KENEK servo-type wave probes (dynamic probes), is used to measure the surface elevation η in the tank. The relative positions of the gauges from the turbine are indicated in Fig. 3(b). The measurements of η are synchronised with the torquemeter data, for a common sampling frequency of $f_e = 512$ Hz. The dynamic probe noted C on the scheme is positioned directly above the turbine at $x = 0$ and serves as the reference for phasing signals of η and turbine characteristics in the subsequent sections. The use of the gauges set also makes the determination of the phase shift between probes possible. By analysing the relative phase between the signals recorded at different longitudinal positions, the wavelength λ of the imposed waves can be estimated. This redundancy also provides a way to check the coherence of the measured signals along the propagation axis and to reduce uncertainty on the incoming wave parameters.

Model description

The model studied is a 1:20 scale prototype of the 2.5 MW-rated machine (Fig. 4(a)), designed by the french company Hydroquest for deployment in the FloWatt tidal farm project at the Raz-Blanchard site (English Channel). The model consists of two vertical rotor columns, also made of two rotor levels arranged with a 60° phase shift. To maintain geometric similarity with the full-scale environment, the model is designed to preserve the ratio between the turbine height and the water column depth in the test tank. The model is H_m= 1.010 m high, for a turbine width w_m = 1.270 m. The rotors are H_b = 0.315 m in height and R = 0.235 m in radius. The rotors are made up of 3 NACA profile blades, H_b = 0.315 m in height and R = 0.235 m in radius. The vertical spacing between the bottom and top plates holding the rotor columns defines the effective turbine height h_m = 0.830 m. The turbine is mounted on a gravity base, which is composed of three weighted arms.

The studied turbine configuration corresponds to a 0° flow-model angle of incidence (Fig. 4(b)), i.e. the main arm of the gravity base is aligned with the flow direction and located upstream from the turbine central pillar. In this configuration, the blades face the incoming flow as they pass near the central pillar, commonly defined as a 'counter-flow' configuration.

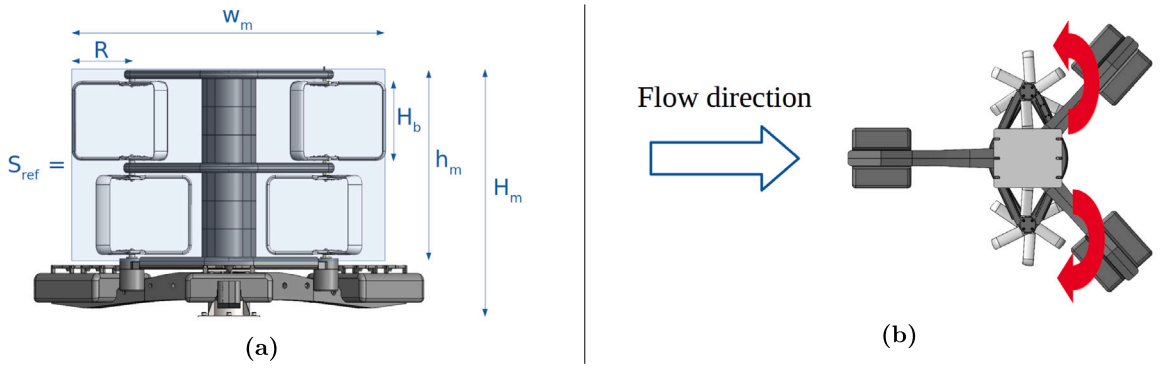


Fig. 4. Model's characteristics. (a) Main dimensions of the model in the (yz) plane. (b) The rotation direction of each rotor column is indicated by the red arrows. The direction of flow relative to the machine is indicated by the arrow.

In order to assess the mechanical characteristics of the turbine during the tests, the control system includes a 26:1 geared motor and a torquemeter SCAIME DR2112, disposed in line with the motorisation below each rotor column to evaluate the column torque noted Q. The motors are also equipped with a high precision encoder (HEDL) for the relative angular position measurements. The system is controlled at a set rotational speed ω for each test, corresponding to a rotors rotation frequency f_ω. The operating mode of the turbine is thus defined as the Tip Speed Ratio or TSR:

$$TSR = \frac{\omega R}{U_0}, \tag{3}$$

which represents the ratio between the tangential blade tip velocity to the inlet flow velocity. The reference area is defined here as the blue surface in Fig. 4(b), representing the projected capture area $S_{ref} = h_m \times w_m$. Based on IEC standards (IEC, 2013), an equivalent diameter D_e is derived from this area: $D_e = \sqrt{\frac{4S_{ref}}{\pi}}$. This parameter can be used to transform a non-circular cross-section machine into an equivalent device with a circular cross-section. The quantities D_e and U_0 are used as reference scales (length and velocity) for normalising the parameters in the study.

Performance of the machine is thus defined from the C_p coefficient and the column torque coefficient C_Q (formulae in (4)). The Fluctuation Intensity (FI) expresses the magnitude of temporal fluctuations relative to its mean value. It is used in this study to characterise the variability of the power and torque coefficients under wave-induced flow conditions.

$$C_p(t) = \frac{Q(t)\,\omega(t)}{\frac{1}{2}\,\rho\,S_{ref}\,U_0^3}\ ,\quad C_Q(t) = \frac{Q(t)}{\frac{1}{2}\,\rho\,S_{ref}\,R\,U_0^2}\ ,\quad FI(\square) = \frac{\sigma(\square)}{\overline{\square}} \tag{4}$$

2.2. Wave characteristics

Four wave conditions are investigated for each tested current velocity (U_0 = [0.6; 0.8] m/s) and are assumed to be monochromatic waves. Three wave cases correspond to waves propagating in the same direction as the current (following the current), while one case involves waves propagating against the current (opposing the current). Cases labelled 'F045' and 'F060' correspond to wave frequencies of f_{wave} = 0.45 Hz and 0.60 Hz respectively. The time range of the measurements is about 140 s, corresponding to N_T = 83 wave cycles for cases with a wave frequency f_{wave} = 0.60 Hz and N_T = 63 wave cycles for cases with f_{wave} = 0.45 Hz. The wave characteristics (frequency, amplitude and phase) are determined from the wave gauges measurements and are given in Table 1. The wavelength is primarily determined from the linear dispersion relation including wave–current interaction effects. Additional phase-based estimations are performed from the phase differences measured between wave probes using a Hilbert-transform approach. For the present experimental configuration, the largest streamwise distance between wave probes located on the same transverse section is approximately 1.20 m. In following wave conditions, the wavelengths predicted from the dispersion relation range approximately from 6 to 10 m, corresponding to $\lambda/\Delta x \approx 5$ to 8 even for the largest available probe separation. The corresponding phase difference $\Delta\phi$ therefore remains limited, ranging from approximately 43° to 72° for the largest probe separation. Such relatively small phase differences make the phase-based estimation of the wavenumber particularly sensitive to phase uncertainties and measurement noise. Consequently, the wavelength values reported for the following-wave conditions are primarily obtained from the wave–current dispersion relation. In opposing-wave conditions, the wavelengths are shorter and the corresponding phase differences over the available probe spacing are larger. The phase-based estimates are therefore more robust and are used as an additional experimental determination.

Table 1
Wave parameters evaluated using the measurements carried out during the tests. Cases labelled F045 and F060 correspond to wave frequencies f_{wave} = 0.45 Hz and 0.60 Hz, respectively. The indices 'A1' and 'A2' denote increasing wave amplitudes at fixed frequency. The suffix 'co' refers to waves propagating with the current, whereas 'opp' denotes waves propagating against the current. The wavelength λ is computed from the linear dispersion relation for following waves and obtained from inter-probe phasing for opposing waves.

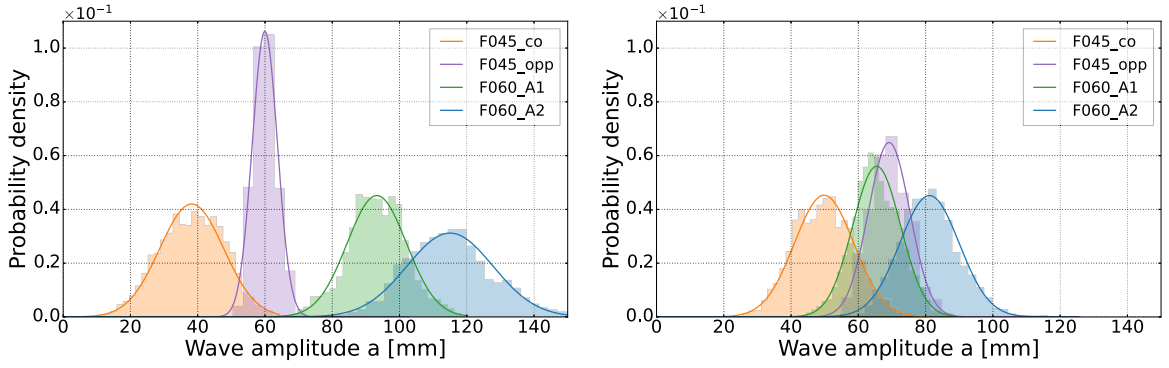
U_0	Wave case	Period T [s]	Height H [m]	Wavelength λ [m]	KC
0.8 m/s	**F045_co**	2.22	0.11	10.1	0.19
	F045_opp	2.22	0.14	4.5	0.07
	F060_A1 (co)	1.67	0.13	6.8	0.14
	F060_A2 (co)	1.67	0.16	6.8	0.18
0.6 m/s	**F045_co**	2.22	0.10	9.4	0.17
	F045_opp	2.22	0.13	4.2	0.12
	F060_A1 (co)	1.67	0.15	6.2	0.14
	F060_A2 (co)	1.67	0.19	6.2	0.18

Based on the geometric similarity and to ensure wave dynamic similarity between the full scale and tank conditions, the Froude number is preserved (Eq. (5)):

$$KC = \frac{u_w\,T}{D_e}\quad ,\quad F_r = \frac{U_0}{\sqrt{g(h-H_m)}} \tag{5}$$

This parameter characterises the balance between inertial and gravitational forces and its preservation validates the correct scaling of wave–current interactions in the experimental setup. The Keulegan–Carpenter number is also given, providing an evaluation of the relative importance of drag and inertia forces induced by the waves on the turbine. In the present experiments, the KC values remain below 0.2, which suggests that drag-driven effects stand predominant over orbital-induced contributions, even if it is not negligible.

The distribution of wave amplitudes ($a = H/2$) measured during the experiments is shown in Fig. 5. The amplitude exhibits a finite temporal variability, with coefficients of variation of approximately



(a) $U_0 = 0.6$ m/s. (b) $U_0 = 0.8$ m/s.

Fig. 5. Wave amplitude distribution for the wave cases, with 63 wave cycles for the waves at $f_{wave} = 0.45$ Hz and 83 wave cycles for the waves at $f_{wave} = 0.60$ Hz. (a) Wave height distribution for $U_0 = 0.6$ m/s. (b) Wave height distribution for $U_0 = 0.8$ m/s.

Table 2
Statistical characteristics of the wave amplitude distributions measured upstream from the turbine ($x = -2.6$ m), at the turbine location ($x = 0$) and downstream from the turbine ($x = 1.1$ m) for the $F060_A1$ case at $U_0 = 0.8$ m/s. The reported ranges correspond to the different TSR investigated.

Probe location [m]	a [mm]	$\sigma(a)$ [mm]	$\sigma(a)/a$ [%]
$x = -2.6$	60-62	8-10	14-16
$x = 0$	55-58	8-9	14-16
$x = 1.1$	54-58	7-9	12-15

15% for the investigated wave conditions. Such variability may result from the combined effects of flow-wave-structure interaction in the flume tank. The contribution of these different mechanisms cannot be precisely separated from the present measurements.

To further assess the spatial variability of the generated wave field, an additional analysis was performed using three wave probes located upstream (at $x = -2.6$ m), at the turbine position ($x = 0$) and downstream (at $x = 1.1$ m) from the turbine. The wave amplitude was obtained from the envelope of the measured surface elevation signal using the Hilbert transform. The mean amplitude and standard deviation obtained at the three locations for the $F060_A1$ case at $U_0 = 0.8$ m/s are reported in Table 2.

The results show that the mean wave amplitude measured upstream of the turbine remains relatively stable over the investigated TSR range, with values between approximately 60 and 62 mm. At the turbine position, the mean amplitude slightly varies from 55 to 58 mm, while the downstream values remain of the same order, between approximately 54 and 58 mm. The standard deviations remain comparable between the three locations, with values generally ranging from approximately 7 to 10 mm. Consequently, no systematic amplification of the amplitude fluctuations is observed between the upstream measurement location and the turbine position for this representative condition. These measurements provide an experimental indication of the finite spatial and temporal variability of the wave field. In particular, the presence of the turbine and its wake modifies the local flow and free surface conditions, which may affect the measured wave amplitude at the turbine position and downstream from the turbine. The differences observed between the probes may therefore result from local flow-wave–structure interactions, in addition to any residual component in the flume tank. These results support the use of the locally measured free surface elevation as the reference excitation for the subsequent analysis, rather than relying exclusively on the nominal wave generation conditions.

The in situ equivalent wave conditions, representative of typical wave events in the Raz-Blanchard (Alderney Race) for this flow-wave incidence (L. Furgerot, 2020), are presented in Fig. 6. The generated wave cases thus cover an equivalent real sea state amplitude range

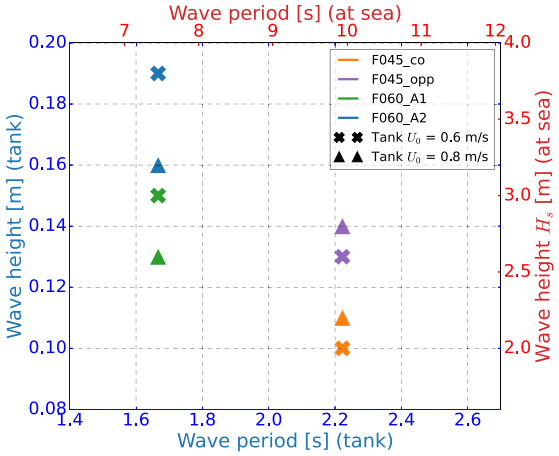


Fig. 6. Wave conditions tested in the tank, with their equivalents at sea. '×' stands for the wave cases generated for a current velocity $U_0 = 0.6$ m/s and the '△' stands for the wave cases under a current velocity $U_0 = 0.8$ m/s.

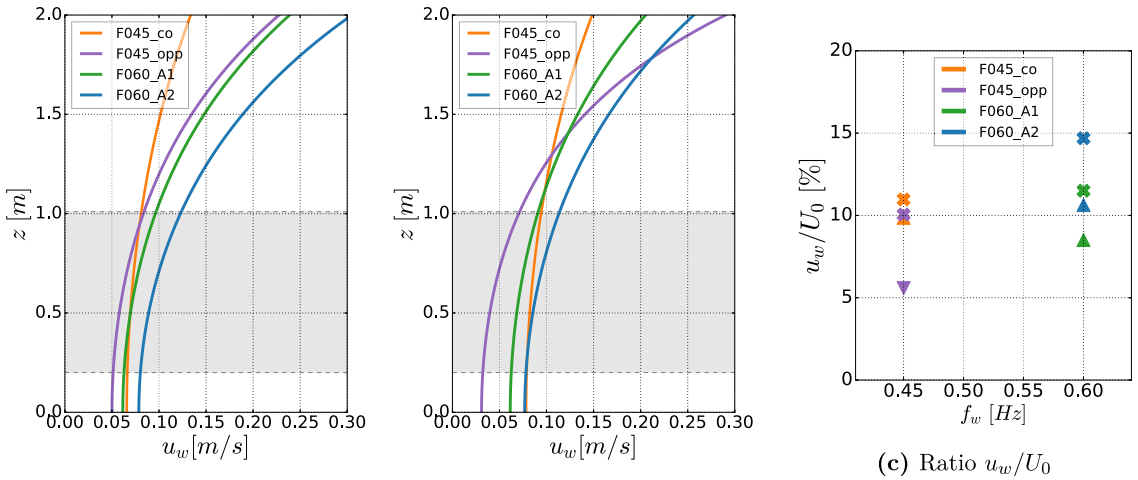
from 2 to 3.5 m high, with period from 7 to 10 s. These parameters are found to be moderate (or even strong) for the conditions assessed at the Raz-Blanchard site. The investigated conditions therefore provide a relevant experimental range for assessing the response of the turbine under combined current and wave loading.

Applied wave theory

To describe the orbital motion induced by surface waves propagation, the Airy wave theory is applied. This approach provides an analytical evaluation of the horizontal and vertical velocity components associated with monochromatic waves. The derivation of these expressions within the framework of linear potential flow theory, including wave–current interaction effects, is detailed in classical wave theory manuscripts such as Dean et al. (1991). For waves of angular frequency $\omega_\phi = 2\pi f$, wavenumber $k = \frac{2\pi}{\lambda}$ and amplitude a, the orbital velocity components $u_w(z,t)$ and $w_w(z,t)$ at the turbine location and for a given depth z (with $z = 0$ at the bottom of the tank and $z = h$ at still water level) are given by:

$$u_w(z,t) = \epsilon\ a\ \omega_{eff}\ \frac{\cosh(kz)}{\sinh(kh)}\ \cos(\omega_\phi t)$$
$$w_w(z,t) = a\ \omega_{eff}\ \frac{\sinh(kz)}{\sinh(kh)}\ \sin(\omega_\phi t) \quad (6)$$

with $\omega_{eff} = \omega_\phi - \epsilon k U_0$ the effective wave pulsation (wave–current effect) and ϵ a coefficient defined as $\epsilon = +1$ for waves following the



(a) $U_0 = 0.6$ m/s (b) $U_0 = 0.8$ m/s (c) Ratio u_w/U_0

Fig. 7. (a)–(b) Examples of the amplitudes of the streamwise orbital velocity profiles (absolute values) obtained for the studied wave cases. The grey area defines the turbine height h_m. (c) Ratios between the average orbital velocity on the turbine height and the reference velocity, called 'orbital ratio' in this paper. '×' stands for the wave cases generated for a current velocity $U_0 = 0.6$ m/s and the '▵' stands for the wave cases under a current velocity $U_0 = 0.8$ m/s.

current and $\epsilon = -1$ for waves opposing the current. The effective wave pulsation ($\omega_\phi - k\epsilon U_0$) accounts for the relative motion between the wave and the background current and so the change of the reference frame ($x_{eff} = x - U_0 t$) (Phillips, 1967), considered to represent the wave Doppler effect. The streamwise and vertical velocity components are expressed without dependence on x, as the analysis focuses on local temporal velocity fluctuations. These expressions make the evaluation of the instantaneous wave-induced velocity field possible at any point in the water column and in our case right upstream of the turbine (Dufour et al., 2026). The applied theory is corroborated by comparing the resulting vertical profiles with PIV measurements (see Appendix A).

Figs. 7(a) and 7(b) displays the subsequent orbital velocity profiles, for the wave cases at $U_0 = 0.6$ and 0.8 m/s. To characterise the influence of wave-induced effects independently of the specific test configurations, an orbital velocity-related parameter, denoted by 'orbital ratio' u_w/U_0, is introduced. This parameter is calculated by averaging the horizontal component u_w amplitude of the orbital velocity, computed using linear wave theory over the entire height of the turbine and thus normalised by the incoming flow velocity U_0. This approach provides a consistent measure of the wave-induced forcing experienced by the machine, enabling meaningful comparisons across different test cases regardless of the exact wave or current conditions. The evaluation of the normalised orbital velocity over the turbine height is presented in Fig. 7(c) for both flow velocities. Three distinct levels of wave influence can be identified based on this ratio. Most wave cases result in a u_w/U_0 representing approximately 10% of the incoming current velocity. However, some configurations show lower influence levels (around 6 to 8%), while an other exhibits stronger effects reaching up to 15%. These variations reflect the combined influence of wave amplitude, frequency and current direction on the resulting orbital motion experienced by the turbine.

2.3. Turbine behaviour under surface waves

The influence of waves on turbine performance is presented for both reference current velocities $U_0 = 0.6$ m/s and $U_0 = 0.8$ m/s. The $U_0 = 0.8$ m/s configuration is yet considered as the main operating condition for the following parts, since it ensures consistent and well-characterised turbine behaviour which provides a robust reference for assessing wave-induced fluctuations. Complementary results obtained for $U_0 = 0.6$ m/s will then also be considered for comparison. For confidentiality reasons, both power and torque coefficients are normalised by their respective maxima evaluated in equivalent steady current conditions, denoted $C_{P,ref}$ and $C_{Q,ref}$.

Temporal acquisition

To first illustrate the nature of the acquired data, Fig. 8 gives a representative example of the free-surface elevation and turbine torque signals. The time window shown corresponds to the portion of the record after a duration of wave formation $t = 40$ s, once the wave field has reached a fully developed regime and the initial transient regime associated is dissipated.

The raw $\eta(t)$ signal measured by the wave probe positioned vertically above the machine exhibits a nearly monochromatic oscillation, with a stable amplitude and frequency. The evaluated parameters are consistent with the imposed wave conditions, despite few inconsistencies related to the probe precision. The raw torque measurement contains several superimposed contributions, comprising the periodic wave-induced modulation (band-pass filtered signal in red), higher frequencies corresponding to the blades motion and then turbulent noise induced by the flow. The wave-related filtered torque exhibits a clear periodicity synchronous with the surface elevation which highlights the wave-induced loading mechanism. This confirms both the regularity of the generated wave train and the repeatability of the hydrodynamic loading applied to the turbine. The cross-correlation function applied to these signals exhibits a strong periodic structure at the imposed wave period, with a pronounced maximum located near zero time lag (about 0.2 s). The absence of significant delay further features the high coupling between the incident wave kinematics and the turbine torque response.

Average power dependence on wave loading

Fig. 9 presents the normalised mean power coefficient C_p of the turbine for the tested wave conditions, along with a reference steady case (REF) without waves. The fluctuation intensity $FI(C_p)$ is also displayed.

The resulting C_P curves closely match those obtained under steady inflow conditions (Saouli et al., 2025), indicating that the mean turbine performance is weakly affected by wave propagation. Three distinct operating regimes can be identified: a low regime for $TSR \leq 1.9$, a transitional regime between 1.9 and 2.4 and a sub-optimal regime in which the power coefficient decreases with increasing TSR. The fluctuation intensity of C_p helps to point out the impact of wave-induced unsteadiness on the power output. The reference case (REF) maintains a consistent $FI(C_p)$ across the range of TSRs tested, while the introduction of wave kinematics leads to a marked increase in fluctuations especially near and beyond the higher optimal operating point. For a flow velocity of $U_0 = 0.8$ m/s, the highest fluctuation level

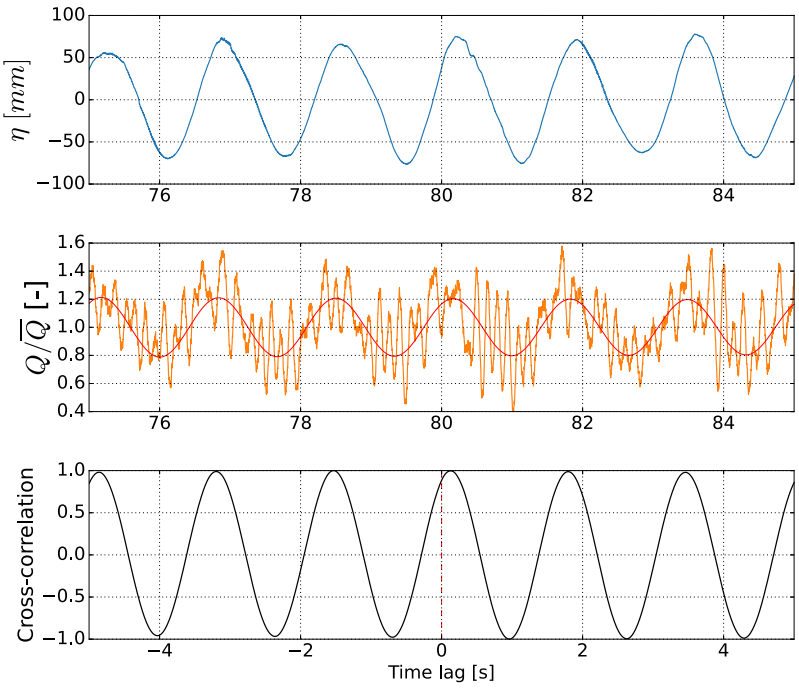
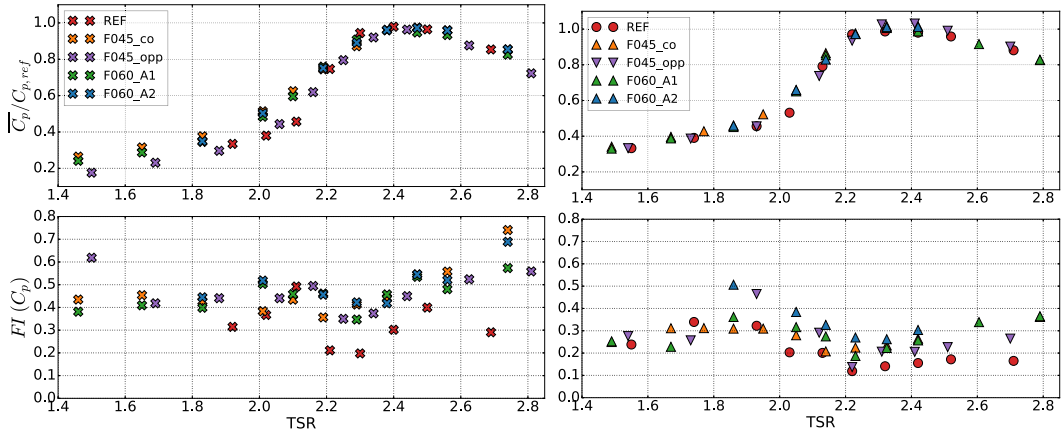


Fig. 8. Raw signals and cross-correlation from the measurements on a 10 s range, at the optimum operating point (TSR = 2.4) under the $F060_A1$ case and $U_0 = 0.8$ m/s. The raw torque signal is displayed in orange, while the filtered torque around the wave frequency $[f_{wave} - 0.05 ; f_{wave} + 0.05]$ is displayed in red. The torque signal is normalised by the mean torque value $\overline{Q}$ of the signal.



(a) $U_0 = 0.6$ m/s (b) $U_0 = 0.8$ m/s

Fig. 9. $\overline{C_P}/C_{P,ref}$ and the FI(C_P) curves for the reference case (no wave) and the four wave cases tested. $C_{P,ref}$ is defined as the maximum power coefficient obtained without waves for each flow velocity U_0.

is observed for the $F060_A2$ case, with $FI(C_p)$ reaching up to 30% of the $\overline{C_p}$ at the optimal TSR. Such elevated unsteadiness highlights the turbine's sensitivity to wave loading in this regime and is in line with the importance of its orbital ratio. Similar levels of fluctuations are observed between the cases $F060_A1$ and $F045_co$ (15% to 20%), despite the $F045_co$ case exhibiting wave amplitudes approximately 15% lower than those in $F060_A1$. At a lower flow velocity $U_0 = 0.6$ m/s, the trends are globally consistent with the previous observations, but with even stronger relative effects: fluctuation intensities reach nearly 50% around the optimal TSR, with similar levels across the different wave cases. Compared to the reference, it represents twice its variability. The relative variations observed for the mean coefficients at TSR ≤ 2.0 for $U_0 = 0.6$ m/s may be partly attributed to differences in the effective flow velocity experienced by the turbine between co-current and counter-current configurations. Although the imposed current velocity remains constant, the local relative velocity used for normalisation and perceived by the rotor differs slightly between both cases due to the setup influence. It may lead to variations in the effective Reynolds number and explains the sensitivity of the results in this turbulent regime (Yamada et al., 2016).

These results underline the importance of accounting for wave-induced unsteadiness when designing control strategies or performance predictions for vertical axis turbines in realistic marine environments. It also suggests that, while average performance might remain comparable in some wave conditions, the increased variability in power output could have important implications for system stability, power grid integration and structural loading.

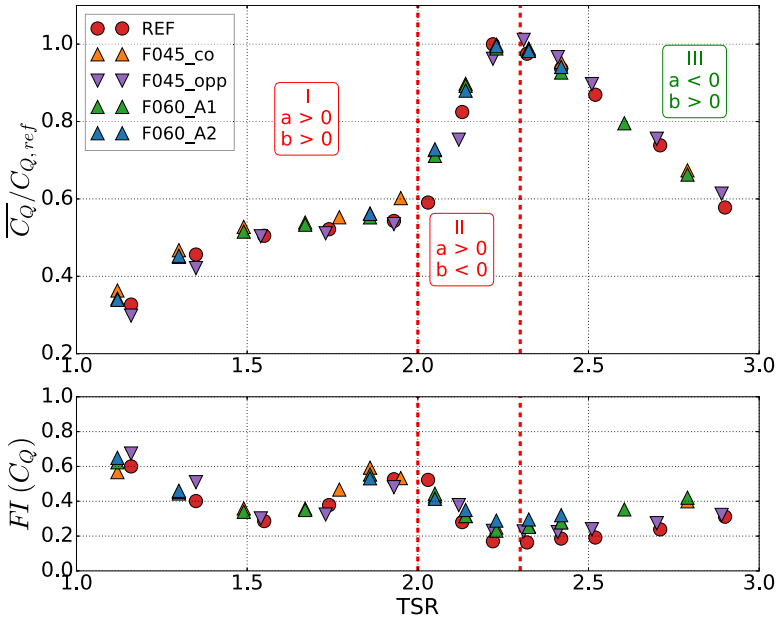


Fig. 10. $\overline{C_Q}/C_{Q,ref}$ and the FI(C_Q) curves for the reference case (no wave) and the four wave cases tested. $C_{Q,ref}$ is defined as the maximum torque coefficient obtained without waves for each flow velocity U_0.

Torque distribution and operating regimes

To complement the analysis of the average performance, the torque dynamics is studied under wave effect as the system is controlled at a set rotational speed ω. As the most reliable and established trends are observed at $U_0 = 0.8$ m/s, the following results are presented for this flow velocity only. The additional results obtained at $U_0 = 0.6$ m/s are yet consistent with the following observations.

Fig. 10 presents the evolution of the phase-averaged torque coefficient $\overline{C_Q}$, normalised by the reference maximum torque coefficient $C_{Q,ref}$, as a function of the TSR. Over the investigated TSR range, it appears that the mean torque coefficient evolution can be approximated by three affine laws of the form:

$$C_Q(TSR) = a.TSR + b \tag{7}$$

corresponding to three distinct operating regimes.

At low TSR values (regime I), the torque coefficient increases with TSR, corresponding to a positive slope ($a > 0$). The regime II corresponds to a transition zone but still shows an even more marked positive slope. Around the optimal TSR, the torque coefficient reaches a maximum and tends to a weak dependence on TSR, with a coefficient plateau almost reached. At higher TSR values (regime III), the torque coefficient decreases with increasing TSR, leading to a negative slope ($a < 0$).

From a dynamic point of view, the stability of the rotor can be interpreted from the rotational equation of motion, i.e. the angular momentum balance (Eq. (8)):

$$J\frac{d\omega}{dt} = Q_h(t) - Q_{load}(t) \tag{8}$$

where J is the rotor column inertia, Q_h is the hydrodynamic torque and Q_{load} represents the resisting torque of the system (especially the applied electrical control).

Considering small perturbations around an equilibrium rotational speed ω_0, the linearised dynamics can be written as:

$$J\frac{d(\delta\omega)}{dt} = \frac{dQ}{d\omega}\delta\omega$$

The stability of the system is therefore governed by the sign of the torque sensitivity $dQ/d\omega$ evaluated at the operating point. Since the tip-speed ratio is proportional to the angular velocity for a given inflow velocity, this criterion can equivalently be expressed in terms of the derivative with respect to the TSR:

$$\frac{dQ}{d\omega} \sim \frac{dQ}{dTSR}$$

As a consequence, the sign of the slope $a = dC_Q/dTSR$ governs the local dynamic stabilisation of the operating point: negative slopes correspond to stable equilibrium, while positive slopes indicate unstable response. Importantly, the same three operating regimes are observed for both the reference case and the wave cases, indicating that the presence of waves does not fundamentally alter the mean operating behaviour of the column when considering periodic loading. However, around the optimal TSR, wave-induced torque fluctuations may lead to excursions towards higher TSR values, potentially bringing the rotors to an uncontrolled state of increasing rotational speed and shifting to a wave-related stability. This highlights the necessity of accurately characterising the mean and periodic wave-induced torque contributions when designing control laws for hydrokinetic turbines operating in wave–current conditions. While the mean torque behaviour provides valuable insight into the global operating regimes and the associated stability, it does not capture the temporal structure of the wave-induced fluctuations. To further investigate the influence of waves on the turbine dynamics, a spectral analysis of the torque signals is therefore conducted.

Spectral analysis

Fig. 11 shows the evolution of the torque spectral distribution over a range of TSRs, representing each operating mode, based on a power spectral density analysis. For all the cases, a distinct component emerges at the wave frequency f_{wave}, whose relative intensity becomes more important as the rotational speed increases. This indicates that the wave-induced fluctuations progressively modulate the torque dynamics as the turbine approaches and exceeds its optimal operating point. Among the configurations, the $F060_A2$ case, which is associated with the highest orbital velocity ratio, exhibits the strongest contribution of the wave frequency. Another noticeable feature is the evolution of rotor-induced harmonics: as TSR increases, the dominant harmonics shift from $6f_\omega$ to $3f_\omega$ with f_ω the rotational frequency, which reflects a change in hydrodynamic behaviour as reported in previous studies involving this technology (Saouli et al., 2025; Linant

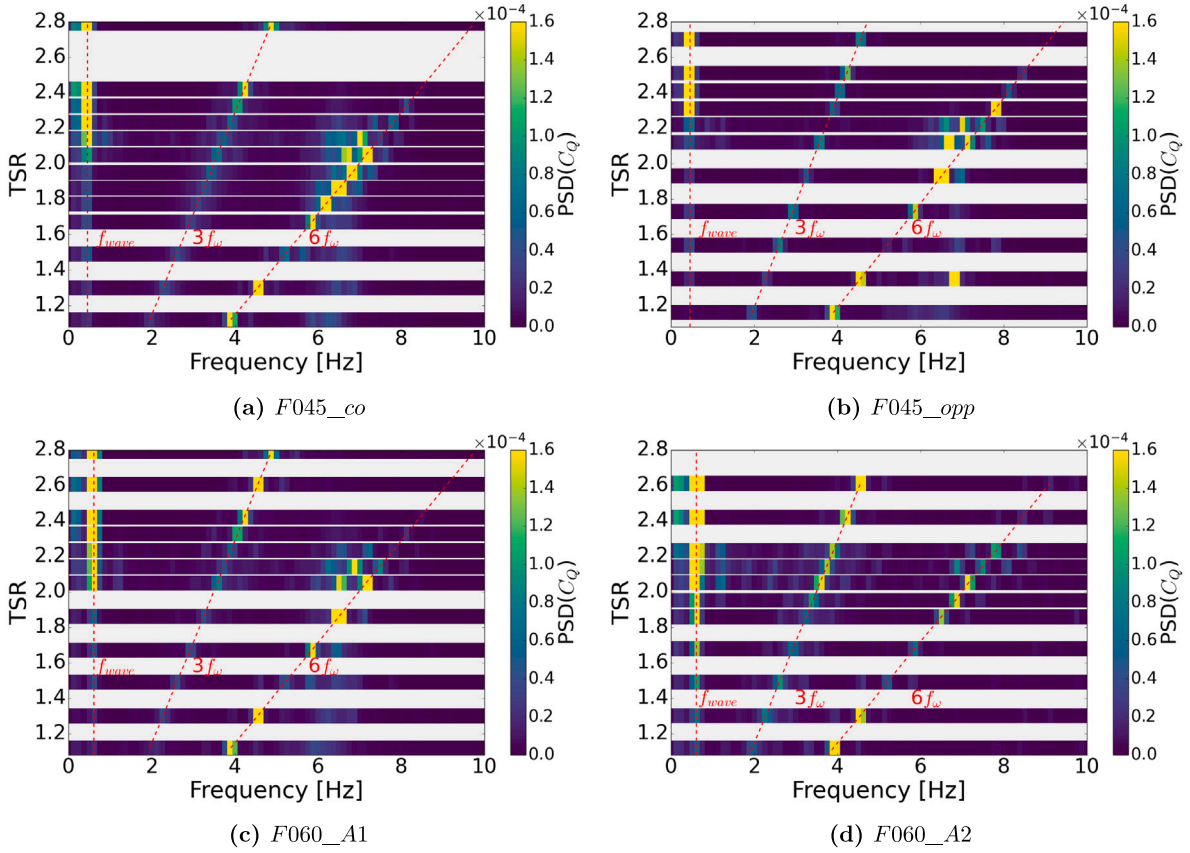


Fig. 11. Power Spectral Density PSD(C_Q) regarding frequency and TSR, for the wave cases tested at $U_0 = 0.8$ m/s.

et al., 2025). This observation is inherent to boundary layer detachment and dynamic stalls for vertical axis turbines depending on the rotation regime of the rotors (Bossard, 2012). At high TSR, the PSD intensity near f_{wave} becomes comparable to, or even exceeds, these rotational components, marking a transition from rotation-dominated to wave-dominated torque fluctuations.

To better illustrate these spectral features and quantify their contribution, the focus is made on specific operating points, representative of the observed operating regimes. The frequency content of the torque signal is also displayed through Fourier analysis. Fig. 12(a) displays the Fourier spectra of the torque signals under the $F060_A1$ case for both TSRs = 1.3 and 2.3. A distinct spectral peak appears at the wave frequency, with amplitude varying according to the operating point. At low TSR (= 1.3), this wave-induced peak remains negligible compared to the rotation-induced harmonics, notably the $6f_\omega$ component. As the TSR increases, the relative contribution of f_{wave} becomes comparable to the rotor harmonics, while at the highest TSRs (= 2.3), the wave component dominates the spectrum as expected from the PSD analysis. The amplitudes of the spectral component at the wave frequency between the wave cases are also consistent with the orbital velocity ratio u_w/U_0, with the weakest response systematically observed in cases with the weakest orbital ratios (i.e. here the $F045_opp$ case). In addition, Fig. 12(b) displays the ratio values between the wave peak and the strongest rotational components selected around $3f_\omega$ and $6f_\omega$. To avoid the non representative components, a condition is imposed to select the highest component around each frequency, particularly relevant when considering the dispersion between the rotational frequencies at TSR = 2.0. An example of the considered frequency bands is displayed in Fig. 12(a) (coloured areas). This quantification confirms the progressive spectral shift: the peak ratio increases consistently with TSR, highlighting the growing influence of wave-induced fluctuations at higher operating speeds. Across all wave cases, the ratio remains below 1 at low TSRs, wave peaks thus remain subdominant. It then becomes comparable to the rotor harmonics (about 1:1) around the optimum and exceeds 2 at TSR = 2.3 in the most energetic cases, confirming the spectral shift from rotation-dominated to wave-dominated torque fluctuations. This trend is consistent across different wave amplitudes and directions (following and opposing wave–current propagation), indicating that TSR plays a dominant role in governing the spectral balance between rotational and wave-induced torque fluctuations. Comparable dynamics are found for the $U_0 = 0.6$ m/s tests, supporting the robustness of these conclusions.

The performance analysis and spectral decomposition highlight the combined influence of rotor dynamics and wave-induced effects on the turbine response. These results also emphasise the importance of accounting for wave-induced loading in the design and operation of VATT systems. The spectral analysis further shows that rotational harmonics and wave-frequency contributions remain clearly distinct in these experiments. The present study therefore focuses on the dominant coherent response associated with f_{wave}, which can thus be isolated from the rotational components using a band-pass filtering procedure.

Wave-related torque distribution

In order to characterise the mechanical response of the turbine under wave conditions, Fig. 13 presents the phase-averaged wave-related torque coefficient $C_{Q,\mathrm{wave}}(\phi)$ plotted against the instantaneous wave-modulated operating point:

$$TSR_{\mathrm{wave}}(\phi) = \frac{\omega R}{U_{\mathrm{wave}}(\phi)}, \qquad C_{Q,\mathrm{wave}}(\phi) = \frac{Q_{\mathrm{wave}}(\phi)}{\frac{1}{2}\,\rho\, S_{ref}\, R\, U_{\mathrm{wave}}(\phi)^2}$$

The wave-related torque Q_{wave} is extracted by filtering the torque signal around the wave frequency band as defined from the previous analyses (band-pass as applied in Figs. 8 and 12(a)). U_{wave} is thus defined as given in Eq. (2) to avoid turbulent-driven components. The representation enables a direct visualisation of the phase-dependent mechanical

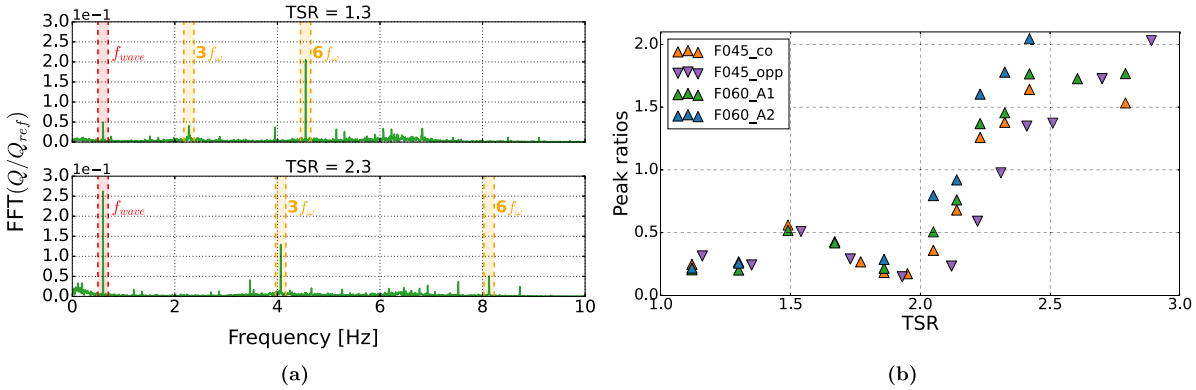


Fig. 12. (a) Fourier transforms of the torque signals for the $F060_A1$ case at $U_0 = 0.8$ m/s. Two TSRs are presented: 1.3 (top) and 2.3 (bottom). (b) Ratios of the FFT peaks between wave and rotational components for the tested range of TSRs. The frequency bands considered for calculating the ratio are displayed in (a).

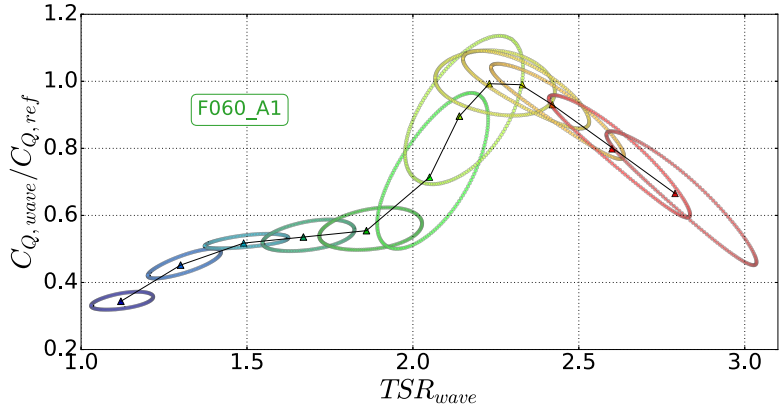


Fig. 13. Phase distribution of the wave-related torque coefficient $C_{Q,wave}$ as a function of TSR_{wave}. The experimental results are here displayed for the $F060_A1$ case and $U_0 = 0.8$ m/s.

response induced by the wave action across the operating range of the turbine. The phase-averaged distributions are obtained from the long-duration experimental time series using a Hilbert-transform-based phase reconstruction. The instantaneous phase ϕ is reconstructed from the filtered surface elevation signal using a Hilbert-transform approach. All measured quantities are subsequently phase-aligned and ensemble-averaged over uniformly distributed phase bins spanning one wave period. Such a procedure isolates the coherent wave-induced response of the turbine while mitigating the influence of turbulent fluctuations and residual low-frequency signal modulation. Similar phase-averaged representations have previously been used for horizontal axis turbines to investigate dynamic loading induced by waves (McNaughton et al., 2025; Guo et al., 2018). Its application to vertical axis tidal turbines, however, remains largely unexplored.

The operating point dynamically explores a range of TSR_{wave} values as a result of the modulation of the incoming flow velocity within the water column. Over a large part of the cycle, the torque coefficient follows the trend of the mean torque coefficient curve $C_Q(TSR)$, shown as the solid line. This trend is consistent with the mean torque coefficient curves presented previously in Fig. 10, as the band-pass filtering used to extract Q_{wave} does not alter the mean component of the signal. To first order, this indicates that the primary effect of waves is a velocity-driven modulation of the turbine operating point along its stationary torque characteristic. However, the phase-averaged trajectories follow distinct hysteresis loops in the $(TSR_{\text{wave}}, C_{Q,\text{wave}})$ phase space. This observation demonstrates that the torque response cannot be described as a quasi-steady function of the instantaneous TSR_{wave}. The presence of these loops reveals additional period-dependent mechanisms, mainly associated with inertia-related effects and temporal lags between flow velocity, orbital acceleration and mechanical torque response. The amplitude and shape of the excursions strongly depend on the mean operating regimes described in . At low TSR (regime I), the trajectories remain narrow and closely follow the mean $C_Q(TSR)$ curve, indicating a weak sensitivity to wave-induced unsteadiness. In contrast, near the optimal operating region (regime II), the phase trajectories widen significantly, reflecting an enhanced sensitivity of the turbine response to wave-induced kinematics. The wave effects may locally increase the torque coefficient by up to approximately 30% relative to its mean value for a given TSR. For the highest TSRs (regime III), the inertia-related effects slowly decrease but the excursions induced by the velocity fluctuations appear more pronounced. Similar hysteretic behaviours have been reported in recent studies on horizontal tidal turbine dynamics under unsteady inflow conditions (McNaughton et al., 2025; Wang et al., 2026), but with distinct modes than those observed in the case of the vertical axis turbine.

These analyses, especially the spectral decompositions of the torque signal, have enabled identification of the dominant mechanisms associated with wave loading and quantification of the induced fluctuations. Nevertheless, they also reveal a fundamental limitation of a purely linear transfer-function description. The phase-space representation provides a compact and physically meaningful description of the wave-turbine interaction. The wave loading simultaneously introduces a modulation of the incident velocity and an inertia-related contribution, both of which contribute to the observed phase distribution and whose relative importance varies with TSR. From a modelling and design perspective, it is therefore necessary to formulate a simple yet physically interpretable framework capable of capturing these mechanisms while explicitly accounting for the dependence on the operating

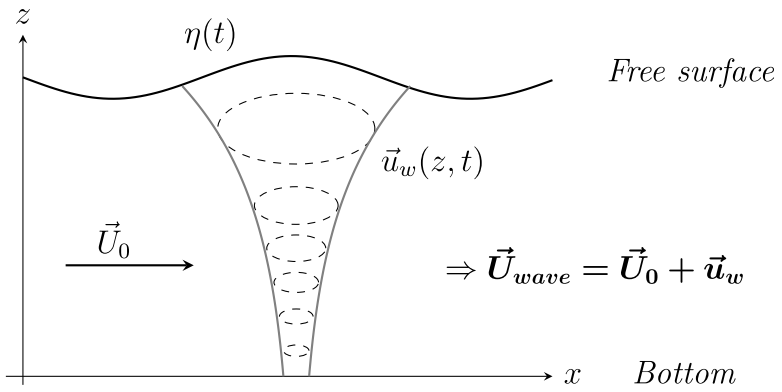


Fig. 14. Vertical section of the water column showing mean current $\vec{U}_0$ and wave orbital kinematics through $\vec{u}_w$. The orbital velocity decays exponentially with depth.

point. In this context, a parametric model inspired by Morison-type formulations is introduced in the following section, allowing the wave-induced torque to be decomposed into hydrodynamic and inertial contributions. Such a model would also enable extrapolation to arbitrary wave conditions by linking the torque response to measurable flow parameters. This capability is essential for extending the analysis from controlled laboratory conditions to realistic sea states.

Building on these findings, the following section proposes an analytical approach aimed at characterising the contribution of wave kinematics to the torque response, thereby enabling a more accurate prediction of output fluctuations.

3. Modelling of wave-induced torque fluctuations on VATT

A parametric formulation is proposed to model the torque fluctuations induced by wave–current interactions. The objective is to capture the main contributions of hydrodynamic forcing and wave-induced kinematics by applying an experimentally-based model.

Fig. 14 summarises the flow decomposition retained for the parametric modelling. The schematic highlights the kinematic quantities governing the wave-related torque response and defines the velocity inputs used in the following formulation. The instantaneous velocity is decomposed into a mean current component $\vec{U}_0$ and a wave-induced orbital component $\vec{u}_w(z,t)$, while turbulent fluctuations $u'(t)$ are not considered at this stage.

3.1. Parametric morison-inspired model

Morison-type formulations are widely used in offshore engineering to represent hydrodynamic loading on rigid bodies exposed to combined current-wave conditions (Morison et al., 1950; Marty et al., 2022). In the spectrum range relevant to tidal turbines, such "hydro - inertia" models (Konstantinidis et al., 2017) have been proven to be robust in the industrial field. For instance, it is used to predict both global loads and local responses of fixed structures like monopile (Húsgard et al., 2020) and jacket foundations (Bai et al., 2025) for offshore turbines subjected to unsteady flows. As part of the assessment of the turbine output fluctuations, this concept is extended to the torque output of a vertical axis turbine. Based on the Morison's equation, a first-order formulation of the wave-related torque can be written as:

$$Q_{\text{wave}}(t) = \underbrace{\tfrac{1}{2}\,\rho\, S_{ref}\; R\, C_{Q,w}\, U_{\text{wave}}(t)^2}_{(Q_h)} \quad \underbrace{+\rho\, V_{ref}\; R\, C_{MQ}\, \frac{dU_{\text{wave}}(t)}{dt}}_{(Q_M)} \tag{9}$$

where $C_{Q,w}$ is the velocity-related coefficient classically defined in steady-state flows (reminder Eq. (4)) and C_{MQ} accounts for the inertial effects related to wave-induced accelerations. The latter is usually associated to an added-mass coefficient ($c_a = C_{MQ}$ - 1) inherent to the studied structure. Fig. 15 schematically illustrates the modelling framework. The quadratic velocity-dependent term Q_h represents the velocity modulation contribution, while the acceleration-dependent term Q_M accounts for inertia-related effects induced by the unsteady wave kinematics. Their superposition results in the wave-related torque Q_{wave} considered for the parametric modelling developed hereinafter.

However, this simplified formulation does not explicitly account for the turbine operating point, whereas the spectral analyses presented in revealed a strong dependence of the torque response on the TSR (Eq. (7)). The mean torque coefficient at a given operating point may therefore be approximated as:

$$\overline{C_Q}(TSR_0) = A.TSR_0 + B \tag{10}$$

where A denotes the local slope of the torque curve, B the corresponding intercept and TSR_0 the mean operating point defined from U_0. This approximation is supported by the quasi-linear trends observed in Fig. 10 over each regime. Under wave loading, the operating condition becomes phase-dependent through the wave-modulated inflow velocity $U_{\text{wave}}(t)$. The instantaneous tip-speed ratio is therefore written as:

$$TSR_{\text{wave}}(t) = \frac{\omega R}{U_{\text{wave}}(t)} \tag{11}$$

Assuming that the velocity-related response preserves the same local affine dependence as in steady conditions, the phase-dependent torque coefficient may be expressed as:

$$C_{Q,w}(t) = A.TSR_{\text{wave}}(t) + B \tag{12}$$

To explicitly relate this expression to the mean operating condition, the instantaneous TSR is decomposed into a mean component and a fluctuating contribution:

$$TSR_{\text{wave}}(t) = TSR_0 + \delta TSR(t), \qquad \delta TSR(t) = TSR_{\text{wave}}(t) - TSR_0$$

Substituting this decomposition into Eq. (12) yields:

$$\begin{aligned} C_{Q,w}(t) &= A\left[TSR_0 + \delta TSR(t)\right] + B \\ &= A.TSR_0 + B + A.\delta TSR(t) \end{aligned}$$

Introducing the coefficients :

$$C_{Q0} = A.TSR_0 + B, \qquad C_{Q1} = A, \tag{13}$$

the torque coefficient can finally be recast as:

$$C_{Q,w}(t) = C_{Q0} + C_{Q1}\left[TSR_{\text{wave}}(t) - TSR_0\right] \tag{14}$$

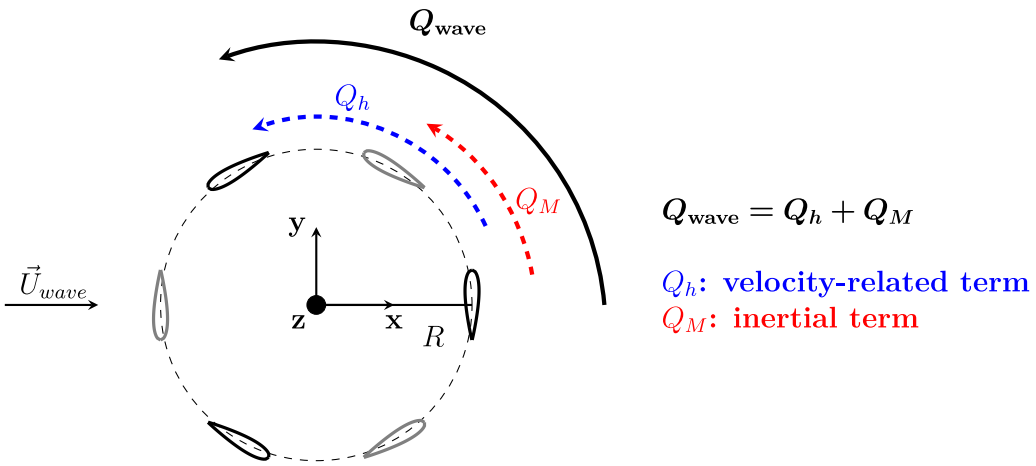


Fig. 15. Top-view schematic of a six-bladed VATT rotor column. The velocity-related term Q_h and the inertial contribution Q_M act about the vertical axis **z** and combine to form the total wave-induced torque Q_{wave}. Blades shown in the same colour belong to the same rotor stage (shifted by 120° relative to each other).

Based on these expressions, the wave-related torque can be expressed as given in Eq. (9):

$$\begin{aligned} Q_{\text{wave}}(t) = & \underbrace{\tfrac{1}{2}\,\rho\, S_{ref}\, R\, C_{Q1}\, \left[TSR_{\text{wave}}(t) - TSR_0\right]\, U_{\text{wave}}(t)^2}_{(1)} \\ & + \underbrace{\tfrac{1}{2}\,\rho\, S_{ref}\, R\, C_{Q0}\, U_{\text{wave}}(t)^2}_{(2)} \\ & + \underbrace{\rho\, V_{ref}\, R\, C_{MQ}\, \tfrac{dU_{\text{wave}}(t)}{dt}}_{(3)} \end{aligned} \tag{15}$$

The expression is thus decomposed into three distinct contributions:

(1) a dynamic term related to the local fluctuations around the average TSR,

(2) an equivalent average velocity-related term,

(3) an inertial term associated to the orbital accelerations.

The C_{Q0} coefficient corresponds to the average torque coefficients obtained in (Fig. 10). The C_{Q1} coefficient governs the torque sensitivity to the TSR variations induced by the waves. In a physical setting, this corresponds to the local gradient of the Q/TSR response activated by the wave dynamics and it can be interpreted as an analogous coefficient of the stability criterium previously established. If the inertial term is first neglected, this expression can be used to analyse the wave-related effects on the regimes stability. The curve slopes obtained with waves (i.e. C_{Q1}) is compared to the average response given by $dC_{Q0}/dTSR$. Doing so, positive values of $C_{Q1} - dC_{Q0}/dTSR$ indicate an increase of the torque fluctuations with the TSR variations (slopes more pronounced with the presence of surface waves), while negative values of the difference correspond to a damping behaviour (decrease of the torque excursions around the mean value). This framework thus provides a unified interpretation based on stability and opens up prospects for the development of control strategies that accommodate the periodic modulation of the operating point induced by waves.

Fig. 16 compares the phase-averaged experimental torque distribution at TSR = 1.8 in comparison with global expression given from Eq. (9) and the extended modelling (Eq. (15)). Fig. 16(a) presents the modelling results obtained for the simplified formula (Eq. (9)) and Fig. 16(b) corresponds to the developed modelling incorporating dependence on the TSR (Eq. (15)). It illustrates the phase structure of the torque response for both formulations. The simplified model hardly reproduces the amplitude of the hysteresis loop observed experimentally, especially overestimating the peak values for this operating point. Similar observations are made to the other TSRs, under/over-estimation depending on the regime. This highlights the relevance of the proposed formulation with a TSR-dependent hydrodynamic coefficients (C_{Q0} and C_{Q1}), which better reflects the interaction between the rotor's motion and the incoming flow. The TSR-dependent model not only improves the amplitude evaluation, but also better captures the phase orientation and sharpness of extrema, supporting its use for more accurate and design-relevant modelling of wave–current loading.

To go further in the modelling description, Fig. 17 presents a detailed physical analysis of the wave-related phase averaged torque for the $F060_A1$ wave case at TSR ~ 1.8. Fig. 17(a) shows the evolution of the wave-related velocity U_{wave} and Q_{wave} over one wave period (in degrees). Characteristic phases are highlighted (every 90°), illustrating the instants of maximum, minimum and zero crossings of the orbital velocity u_w. This figure particularly illustrates the phase difference between the velocity modulation and the resulting torque. In Fig. 17(b), the elliptical shape of the torque response reflects the combined contributions of the velocity-related terms (C_{Q0}, C_{Q1}) and the inertial term (C_{MQ}). The red markers indicate the same characteristic phases as in Fig. 17(a), providing a direct view of the temporal velocity fluctuations and the torque response in the phase-averaged representation. An extremum of the orbital velocity correctly induces an extremum of the U_{wave} component, which does not correspond here to a torque extremum as imposed by the phase difference of the inertial effect. The angle between the horizontal axis and the equivalent major axis of the distribution is defined as $\Delta\Phi$ and can be useful to describe the wave parameter effect on the ellipse phase orientation and thus the relative impact on the torque fluctuations. This dual representation presents the way that the torque fluctuations arise from the interaction of the turbine with wave-induced fluctuations and makes a clear attribution of the elliptical deformation to the distinct contribution terms.

Fig. 18 thus shows the phase-averaged reconstructed torque based on TSR_{wave}. The hydrodynamic (C_{Q0}, C_{Q1}) and inertial (C_{MQ}) coefficients are obtained using a non-linear least-squares fit between the measured torque and the modelling. It should be noted that, for this figure and the remainder of the study, the normalised torque value derived from the extended Morison model will be studied. For each operating point tested, it appears that modelling using empirical mean coefficients accurately reproduces the mean phase of the torque over a wave cycle. For the remainder of the study, the representations will be based on the distributions obtained from the extended Morison formulation of Eq. (15).

Convergence analysis of the extracted coefficients

To assess the robustness and repeatability of the Morison-like torque decomposition, a dedicated convergence analysis is performed using

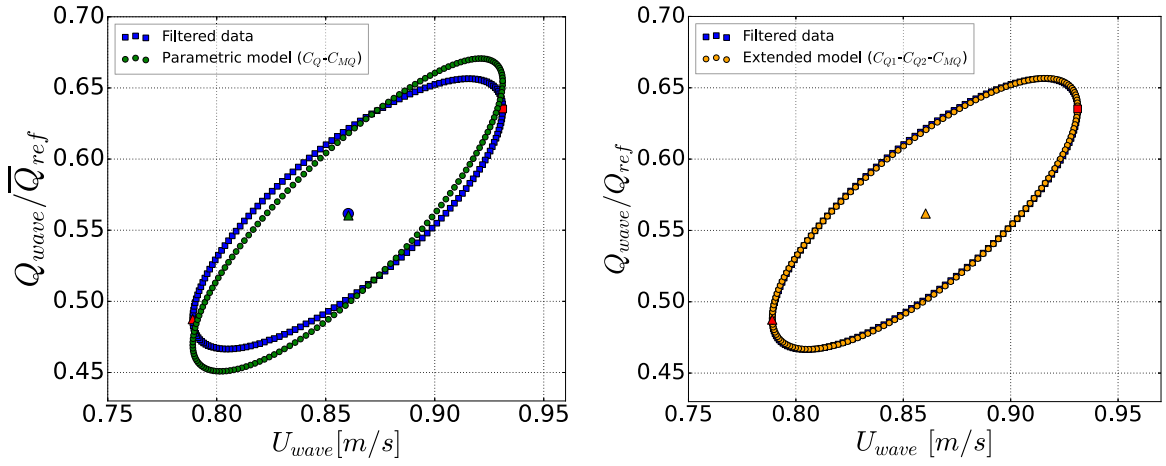
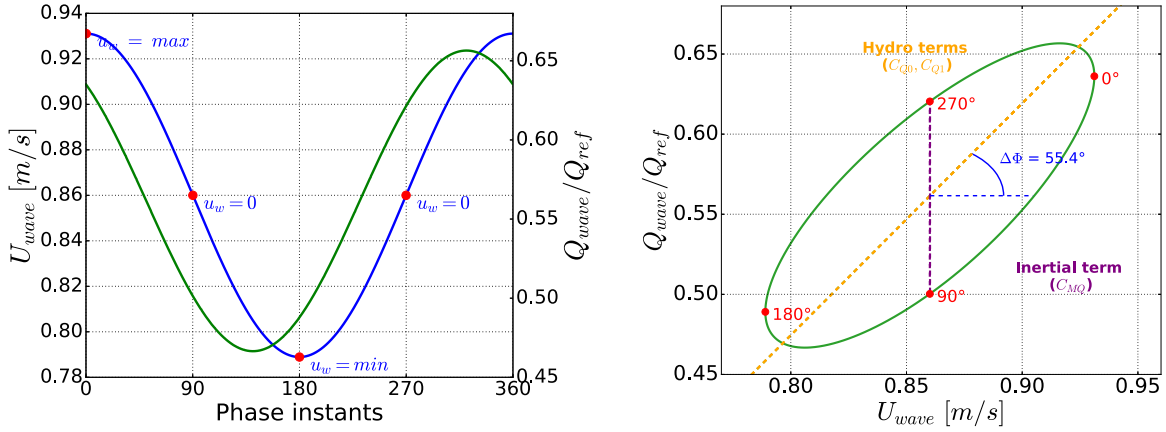


Fig. 16. Wave-related torque fluctuations at TSR ~ 1.8, for the F060_A1 wave case. (a) Modelling using the formulation from Eq. (9). (b) Modelling obtained using the formulation given by Eq. (15) (with the empirical coefficients C_{Q0}, C_{Q1} and C_{MQ}).



(a) U_{wave} (blue) and Q_{wave}/Q_{ref} (green) phases

(b) Phase-averaged $Q_{\mathrm{wave}}/Q_{ref}$

Fig. 17. Physical analysis of the wave-related torque fluctuations at TSR ~ 1.8, for the F060_A1 wave case. Contribution terms from Eq. (15) can be attributed to the elliptical shape and phase orientation.

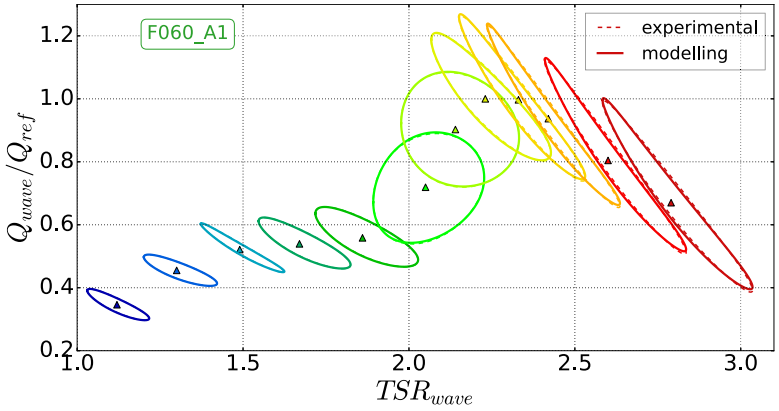
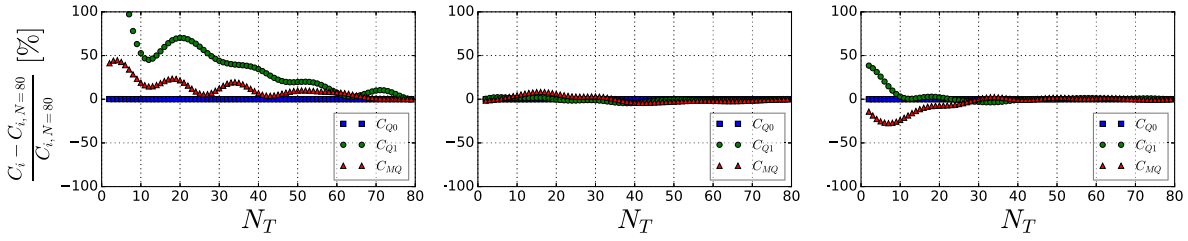


Fig. 18. Comparison of the experimental torque (dots) and modelling-related torque (solid line) distributions induced by the waves. The results are obtained for the $F060_A1$ case, at $U_0 = 0.8$ m/s.



(a) TSR = 1.3 (b) TSR = 2.0 (c) TSR = 2.3

Fig. 19. Convergence of the model coefficients as the relative error to the value obtained considering the 80 wave periods, for the $F060_A1$ case at $U_0 = 0.8$ m/s. The values are here displayed every 2 wave cycles.

the measurements from the case $F060_A1$. It is considered that these coefficients may depend on the duration of the analysed time window. Using too few wave periods may lead to strong variability due to the transient nature of the mechanical response and to the limited statistical representativity of the sample. Conversely, using excessively long acquisition windows may introduce contamination from reflected wave patterns or natural modes in the tank, generating slow drifts in the operating conditions and affecting the identification.

To quantify this sensitivity, the coefficients were recomputed for an increasing number of wave cycles N_T, ranging from a minimum of 2 waves up to 80 waves. For each value of N_T, a time segment centred on the selected N_T consecutive wave periods is extracted and the model coefficients are identified independently. Their evolution as a function of N_T therefore provides a direct assessment of the convergence behaviour.

To evaluate the residual variability at each N_T, a moving average and the associated standard deviation are computed, yielding confidence intervals on the extracted coefficients. Such information is essential for determining the minimum number of wave cycles required to obtain statistically reliable Morison model coefficients. In Fig. 19, the relative error to the value obtained considering the 80 wave periods is displayed. Across the tested operating points, the results indicate that most coefficients reach a stable value once approximately 30 to 40 wave periods are included in the regression. For smaller N_T, some deviations may occur for specific TSR values, particularly at low TSRs. It may be attributed to the lower magnitudes encountered for these TSRs, hence more sensitive to noise and drifts around the mean value. Nevertheless, after the 30 to 40 waves range, the coefficients show limited sensitivity to N_T, as most of the coefficients present less than 5% difference with the value obtained for $N_T = 80$. It confirms the stability of the identified parameters throughout this study, with about 60 to 80 wave cycles regarding the cases tested.

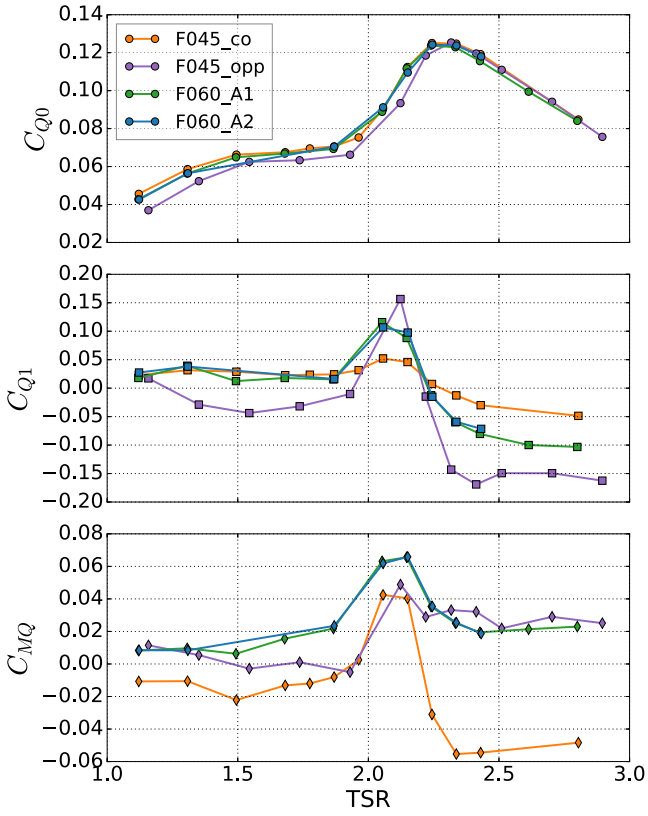


Fig. 20. Coefficients sets (C_{Q0}, C_{Q1}, C_{MQ}) obtained for the TSR range and the wave conditions tested for $U_0 = 0.8$ m/s.

3.2. Physical interpretation of the torque dynamics

After establishing the consistency and robustness of the modelling coefficients, the parameter sets (C_{Q0}, C_{Q1}, C_{MQ}) are now displayed for the tested wave conditions presented in Section 2.2. This part aims to physically interpret their evolution as a function of the TSR to characterise the local dynamics and stability regimes induced by the waves.

Coefficients evolution at $U_0 = 0.8$ m/s

For the highest flow velocity $U_0 = 0.8$ m/s (Fig. 20), the evolution of the mean torque coefficient C_{Q0} closely follows the stationary coefficient curve. A maximum is observed around the optimal performance TSR, with a slight shift towards higher TSR values depending on the wave configuration. This confirms that, even under wave effect, the turbine follows similar regimes than in the stationary conditions, depending on the operating point.

The coefficient C_{Q1} exhibits a pronounced dependence on the TSR. In the sub-optimal regime, C_{Q1} remains small, indicating a weak coupling between wave-induced TSR fluctuations and torque response. In contrast, near the optimal operating region, C_{Q1} reaches large positive values, revealing a strong amplification of torque fluctuations induced by wave kinematics. This behaviour can be attributed to an enhanced interaction between orbital velocity variations and the turbine rotational dynamics when the ratio between orbital and incoming flow velocities remains significant. Beyond the optimal TSR, C_{Q1} becomes strongly negative, indicating a stabilising response of the turbine in the over-optimal regime. In this region, wave-induced TSR excursions tend to amplify torque fluctuations around the mean C_Q curve, consistently with classical stationary stability arguments based on the negative slope of the $C_Q(TSR)$ curve (Fig. 10).

The inertial coefficient C_{MQ} displays a sharp peak around the optimal TSR, highlighting the significant role of orbital acceleration when the turbine operates close to maximum efficiency. Although the relative orbital velocity decreases with increasing flow velocity,

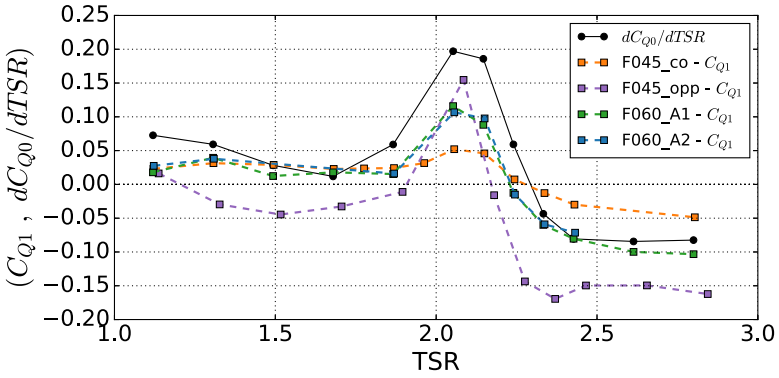


Fig. 21. Comparison of C_{Q1} evolution (dots) with the gradient $dC_{Q0}/dTSR$ of the $F060_A1$ case (solid line) for $U_0 = 0.8$ m/s.

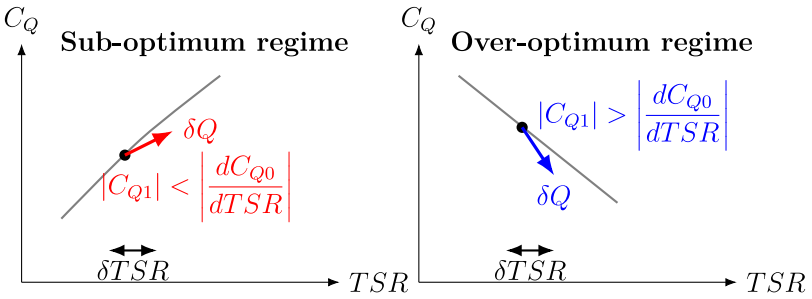


Fig. 22. Conceptual illustration of the effect of wave-induced TSR fluctuations on torque stability, depending on the operating regime. The solid line represents the mean C_Q curve trend as a function of the TSR. δQ represents the torque variation and δTSR the equivalent operating point evolution.

acceleration effects remain substantial and contribute noticeably to the unsteady torque response in this regime. At higher TSR values, C_{MQ} decreases, confirming the secondary role of inertial effects in strongly over-optimal conditions.

To further analyse the influence of waves on the torque regime stability, Fig. 21 compares the evolution of the coefficient C_{Q1} with the gradient of C_{Q0} relative to the TSR. The aforementioned gradient, noted $dC_{Q0}/dTSR$, gives the trends of the stationary regimes and can thus be interpreted as a stability criterion. Indeed, the local slope of the curve $C_Q(TSR)$ directly leads to the amplification or damping of torque variations at each operating point. Since the coefficients C_{Q0} identified under different wave conditions present similar values between the cases and correspond to almost equivalent TSRs (as observed in Fig. 21), only the gradient curve of C_{Q0} for the $F060_A1$ case is displayed in the figure (solid line). The coefficient C_{Q1} can then be interpreted as the effective dynamic slope activated by the waves.

The proposed scheme in Fig. 22 aims to qualitatively illustrate the role of the stationary slope $dC_{Q0}/dTSR$ and the dynamic coefficient C_{Q1}. In Fig. 22 left hand side, when $|C_{Q1}|$ remains lower than $|\mathrm{d}C_{Q0}/\mathrm{d}TSR|$, the TSR excursions imposed by the waves tend to be dampened in the torque response, leading to a reduction in variations along the average curve C_Q. This behaviour is consistent with the classic stability arguments associated with a negative local slope of the torque coefficient. Conversely, in Fig. 22 right hand side, when C_{Q1} becomes comparable to or greater than the gradient of C_{Q0}, the waves activate a more sensitive dynamic response than that predicted by the average steady-state behaviour, reflecting a local regime of torque fluctuation amplification. This comparison thus highlights the role of C_{Q1} as a relevant indicator of dynamic stability under wave action, directly related to the properties of the $C_Q(TSR)$ curve.

Coefficients evolution at $U_0 = 0.6$ m/s

At $U_0 = 0.6$ m/s (Fig. 23), similar qualitative trends are observed, although with reduced amplitudes. The coefficient C_{Q0} exhibits the same evolution than the mean torque coefficient with TSR, a maximum being reached around $TSR \approx 2.1$ in agreement with stationary performance measurements.

The evolution of C_{Q1} reveals a progressive transition across operating regimes. In the sub-optimal range, C_{Q1} remains close to zero, indicating that wave-induced TSR fluctuations have a limited impact on torque dynamics. As the turbine approaches its optimal operating point, C_{Q1} becomes positive and reaches a maximum which reflects an increased sensitivity to wave-induced kinematic excitation. For TSR values beyond the optimum, C_{Q1} decreases and eventually becomes negative, marking the transition towards a dynamically stable over-optimal regime. Compared to the $U_0 = 0.8$ m/s case, the magnitude of C_{Q1} remains lower, which can be attributed to the reduced coupling between orbital velocity and turbine rotation at lower incoming flow velocities. The comparison between C_{Q1} and the gradient $\mathrm{d}C_{Q0}/\mathrm{d}TSR$ (Fig. 24) supports this interpretation. The magnitude of $|C_{Q1}|$ remains globally smaller than $|\mathrm{d}C_{Q0}/\mathrm{d}TSR|$ up to the optimal TSR value, indicating that the TSR excursions imposed by wave-induced velocity fluctuations are attenuated in the torque response. Beyond the optimal TSR, both C_{Q1} and $\mathrm{d}C_{Q0}/\mathrm{d}TSR$ become negative, corresponding to the classically stable over-optimal operating regime. When $|C_{Q1}|$ exceeds the absolute value of the stationary gradient $|\mathrm{d}C_{Q0}/\mathrm{d}TSR|$, the dynamic torque response to wave-induced TSR fluctuations becomes stronger than that predicted by the quasi-steady behaviour. This configuration corresponds to enhanced damping of TSR perturbations: TSR excursions generate torque variations that oppose the imposed disturbance more effectively, thereby increasing TSR stability while producing larger torque oscillations. The inertial coefficient C_{MQ} remains positive over the entire TSR range and exhibits a pronounced peak near to the optimal TSR. This indicates that, at lower flow velocities, orbital acceleration effects play a relatively more significant role in the torque response, consistent with the larger ratio between wave-induced and mean flow velocities.

Overall, the combined evolution of C_{Q0}, C_{Q1} and C_{MQ} highlights the dual role of surface waves: while their impact on the mean torque level remains limited, they strongly modulate the local dynamic response of

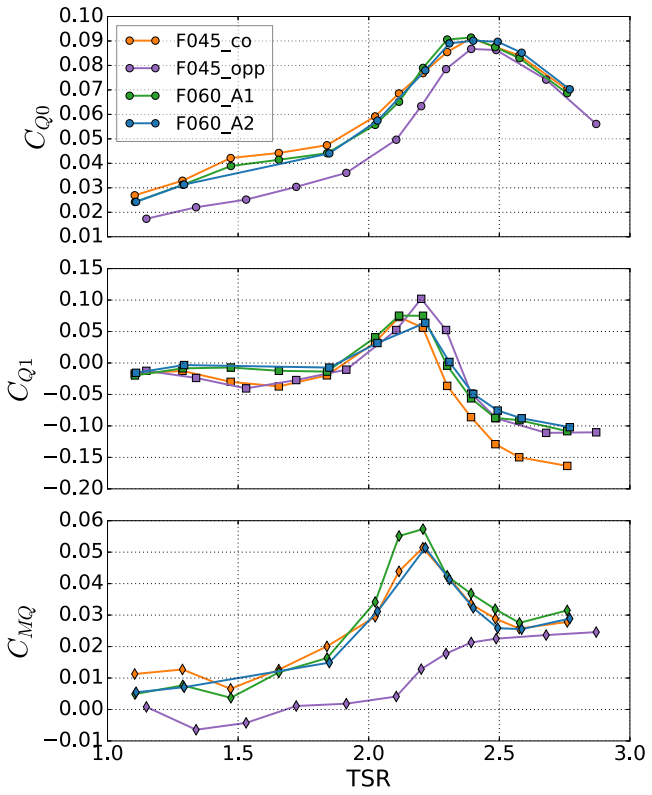


Fig. 23. Coefficients sets (C_{Q0}, C_{Q1}, C_{MQ}) obtained for the TSR range and the wave conditions tested for $U_0 = 0.6$ m/s.

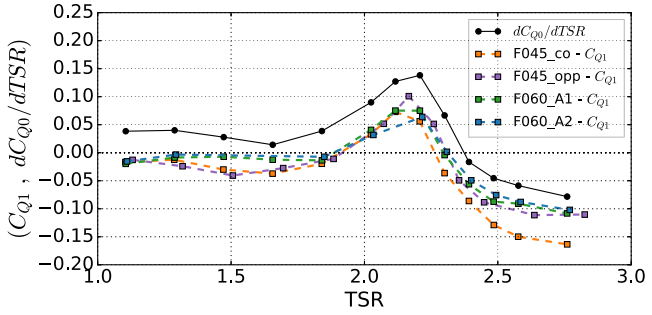


Fig. 24. Comparison of C_{Q1} evolution (dots) with the gradient $dC_{Q0}/dTSR$ of the $F060_A1$ case (solid line) for $U_0 = 0.6$ m/s.

the turbine through TSR-dependent sensitivity and inertial effects. The coefficient C_{Q1} emerges as a key indicator of wave-induced dynamic stability, providing a direct link between unsteady wave loading and classical stationary performance regimes.

Influence of the wave parameters

After analysing the evolution of the modelling coefficients and their physical meaning, it is relevant to examine the influence of wave parameters on torque distribution in the (TSR_{wave}, Q_{wave}/Q_{ref}) framework, based on the extended Morison model. This complementary approach makes it possible to link the observed variations in velocity and inertial coefficients to measurable changes in torque response and to assess how wave characteristics modulate the local dynamics of the turbine. This study is conducted here for wave cases generated at $U_0 = 0.8$ m/s.

Table 3
Wave parameters evaluated using the measurements carried out during the tests ($U_0 = 0.8$ m/s) for the $F060_A1$ and $F060_A2$ cases.

Wave case	Period T [s]	Height H [m]	Wavelength λ [m]	u_w/U_0 [%]
F060_A1	1.67	0.13	6.8	8.5
F060_A2	1.67	0.16	6.8	10.5

Table 4
Wave parameters evaluated using the measurements carried out during the tests ($U_0 = 0.8$ m/s) for the $F045_co$ and $F060_A1$ cases.

Wave case	Period T [s]	Height H [m]	Wavelength λ [m]	u_w/U_0
F045_co	2.22	0.11	10.1	10
F060_A1	1.67	0.13	6.8	8.5

3.2.1. Wave amplitude effect

In this part, the effect of wave amplitude is studied, with wave period and propagation direction similar between both cases in order to isolate the orbital kinematic impact on the torque. Table 3 summarises the wave characteristics used in this subsection.

The wave conditions investigated correspond to monochromatic waves of identical period, while the wave height is varied to modify the orbital velocity amplitude. $F060_A1$ and $F060_A2$ cases have the same wave period ($T = 1.67$ s) and wavelength ($\lambda \sim 6.8$ m), whereas the wave height increases from $H = 0.13$ m to $H = 0.16$ m. This results in a moderate increase in the orbital ratio, from $u_w/U_0 = 8.5$ % to 10.5 % which corresponds to an increase of 20 %.

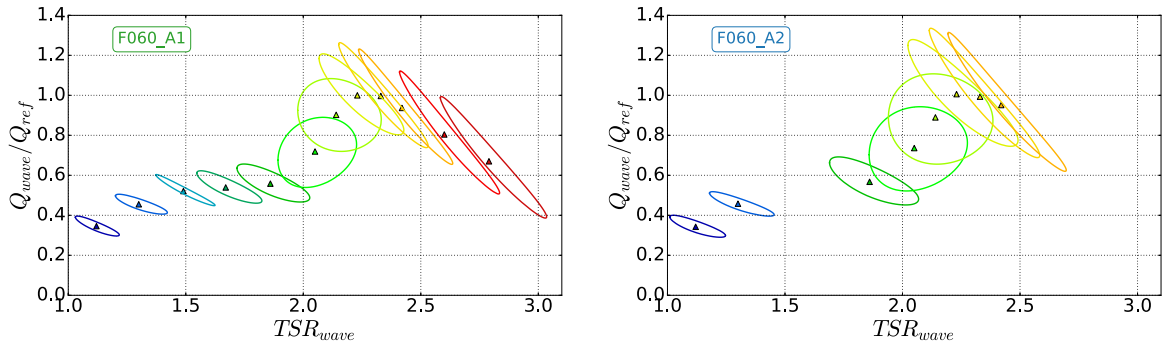
Fig. 25 shows the torque distribution related to the wave average phase for the $F060_A1$ and $F060_A2$ cases. The two distributions show a similar overall organisation across the range of TSR_{wave} considered. The characteristic structures are preserved at each operating point, reflecting an identical dynamic mechanism of torque modulation by the waves.

Fig. 26 shows the distributions around a given operating point $TSR \approx 2.3$. This representation allows for a more detailed comparison of the turbine response for the two wave amplitudes considered. It can be observed that both distributions preserve the same orientation ($\Delta\Phi \approx -54°$) and the same relative organisation in the (TSR_{wave}, Q_{wave}) space, indicating that the phase relationship between the wave-induced kinematics and the torque response remains unchanged. The main difference between the two cases lies in the amplitude of the torque fluctuations around the mean value. The $F060_A2$ case, associated with a higher wave height, results in larger excursions of both torque and TSR_{wave}. This amplification is directly related to the increase in the orbital velocity ratio u_w/U_0, which characterises the relative intensity of the orbital velocity compared to the incoming current velocity. Between these two cases, the increase in wave height leads to an approximately 20% rise in this ratio, which is consistent with the expansion coefficient computed between the two ellipses.

These results therefore show that, at constant wave frequency, the wave amplitude does not alter the dynamic structure of the turbine response, but mainly acts as an amplification factor for the fluctuations of the considered quantities. This observation is also consistent with the model coefficients, which remain nearly identical in both cases. The local dynamics are governed by the same underlying mechanisms, while the intensity of the response is directly driven by the imposed excitation (orbital velocity).

3.2.2. Influence of the wave frequency

$F045_co$ and $F060_A1$ cases differ mainly by their period and wavelength which leads to distinct orbital ratios u_w/U_0. Table 4 summarises the wave conditions considered at the same current velocity ($U_0 = 0.8$ m/s) with varying wave frequency. The longer-period case $F045_co$ produces a slightly higher orbital ratio ($u_w/U_0 \approx 10$ %) than the $F060_A1$ (about 8.5 %). The torque response is then analysed through phase-averaged orientation in the (TSR_{wave}, Q_{wave}/Q_{ref})



(a) $F060_A1$ (b) $F060_A2$

Fig. 25. Phase-averaged torque distribution Q_{wave}/Q_{ref} as a function of TSR_{wave} for both $F060_A1$ and $F060_A2$ cases at $U_0 = 0.8$ m/s.

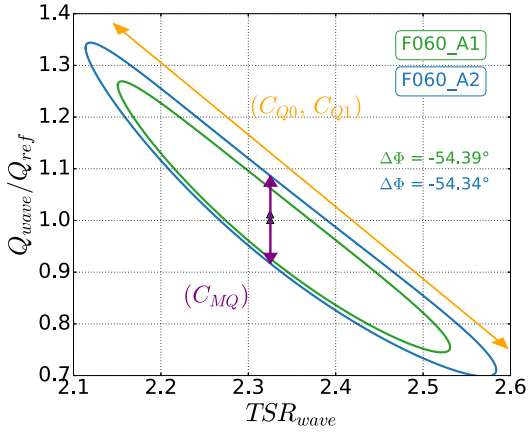


Fig. 26. Comparison of the torque distributions for the $F060_A1$ and $F060_A2$ cases, TSR ≈ 2.3.

space. Fig. 27 presents, for the two considered wave frequencies, the domain covered by the wave-induced torque component.

For an identical operating point, the distributions associated with the longer-period case ($F045_co$) cover a wider region in the (TSR_{wave}, Q_{wave}/Q_{ref}) space than those of the $F060_A1$ case. This difference is consistent with the higher orbital velocity ratio, reflecting stronger fluctuations of the instantaneous inflow velocity and, consequently, a more intense hydrodynamic modulation of the torque. Beyond this scaling effect, the comparison also highlights a specific influence of wave frequency on the inertial contribution. Despite a lower wave height, the $F045_co$ case exhibits torque variations that are comparable to, or even greater than, those of $F060_A1$ over some operating ranges. This behaviour is consistent with an increased contribution of the inertial term, proportional to the orbital acceleration, which scales with wave period for a given orbital velocity amplitude.

The overall organisation of the distributions nevertheless remains very similar in both cases. Fig. 28 presents the Q_{wave} distributions in the vicinity of TSR ≈ 2.3. The measured phase shifts evolve between the two cases but remain close, indicating a moderate change in the dynamic response with wave frequency. Thus, the increase in the orbital velocity ratio u_w/U_0 mainly acts as an amplification factor for hydrodynamic torque fluctuations, whereas the modification of wave frequency influences the balance between quasi-steady and inertial mechanisms. The differences observed for the longer-wavelength case may also involve nonlinear interactions, particularly with respect to water depth effects and basin confinement, which are not fully captured by a purely local representation at turbine height.

Table 5
Wave parameters evaluated using the measurements carried out during the tests ($U_0 = 0.8$ m/s) for the $F045_co$ and $F045_opp$ cases.

Wave case	Period T [s]	Height H [m]	Wavelength λ [m]	u_w/U_0
F045_co	2.22	0.11	10.1	10
F045_opp	2.22	0.14	4.5	5.5

In summary, varying the wave frequency modifies the torque dynamics primarily by adjusting the relative contributions of velocity-related and inertial effects, while preserving the overall organisation of the response. This consistency constitutes a key element for extending Morison-type models to a range of wave–current conditions.

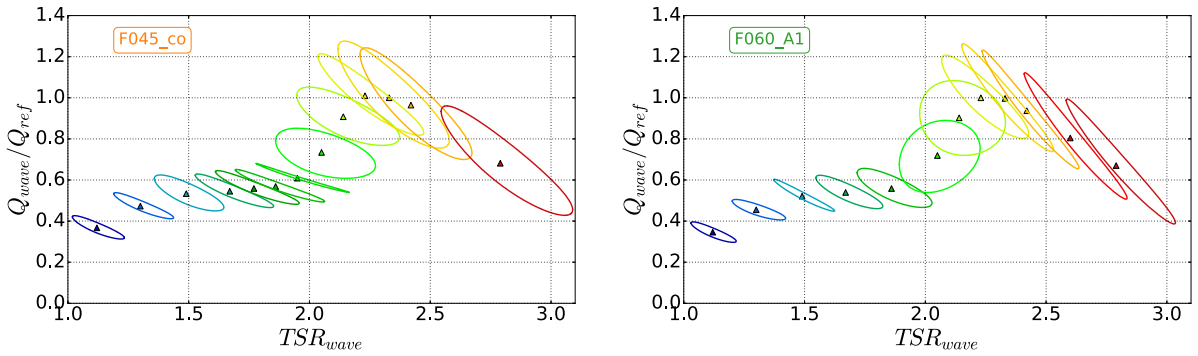
3.2.3. Distribution regarding the wave–current direction

The influence of the wave propagation direction relative to the current is investigated by comparing the $F045_co$ and $F045_opp$ cases, whose main parameters are summarised in Table 5. The experiments are conducted at identical current velocity ($U_0 = 0.8$ m/s) and wave period ($T = 2.22$ s), allowing the sole effect of wave–current incidence on the turbine response to be isolated.

When waves propagate in the same direction as the current ($F045_co$), orbital velocities remain significant over the full turbine height, leading to a local orbital ratio of approximately $u_w/U_0 \approx 10$ %. In contrast, in the opposing current configuration ($F045_opp$), the mean current strongly attenuates the near-bed orbital motion, reducing the orbital ratio perceived at turbine height to about 5.5%. Such a reduction directly implies a weaker modulation of the inflow velocity and therefore a reduced wave-induced torque contribution.

Fig. 29 shows the phase distributions of the dimensionless torque Q_{wave}/Q_{ref} as a function of TSR_{wave} for both propagation directions, while Fig. 30 provides a focused comparison near TSR ≈ 2.3. The distributions indicate that, in the co-current configuration ($F045_co$), the torque response remains strongly modulated by orbital kinematics, producing marked excursions in the (TSR_{wave}, Q_{wave}/Q_{ref}) space. Conversely, in the opposing configuration ($F045_opp$), the distribution collapses onto a much narrower domain, reflecting the reduced amplitude of wave-induced fluctuations.

At TSR ≈ 2.3 (Fig. 30), this contrast becomes particularly evident. The $F045_opp$ case exhibits an almost degenerate elliptical structure, indicating that the inertial contribution associated with orbital acceleration is negligible and that the response is predominantly governed by quasi-steady and velocity-dependent terms. In contrast, the $F045_co$ case retains a well-developed elliptical structure, characteristic of a persistent coupling between drag-like and inertia-like contributions. These observations demonstrate that surface wave parameters alone (height, period, direction) are insufficient to characterise the turbine torque dynamics. Instead, the local orbital ratio u_w/U_0, evaluated at



(a) $F045_co$ (b) $F060_A1$

Fig. 27. Phase distributions of the torque Q_{wave}/Q_{ref} as a function of TSR_{wave} for the two wave cases $F045_co$ and $F060_A1$ at $U_0 = 0.8$ m/s.

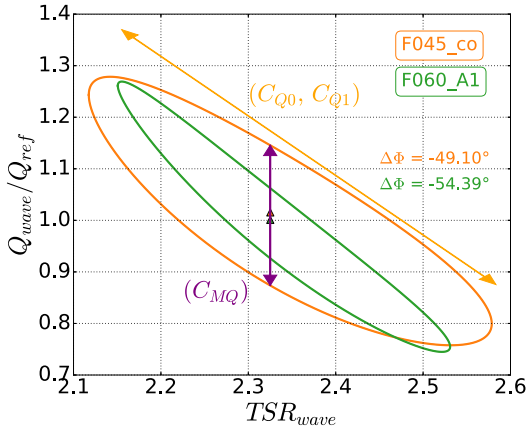


Fig. 28. Comparison of the torque distributions for the $F045_co$ and $F060_A1$ cases, TSR ≈ 2.3.

turbine height, emerges as the relevant similarity parameter controlling the effective wave-induced forcing.

Beyond the geometrical differences highlighted by the ellipse shapes, the phase lag $\Delta\phi$ provides additional insight into the underlying dynamical mechanisms. At TSR ≈ 2.3, $\Delta\phi$ reaches approximately −62° for $F045_opp$, compared to −49° for $F045_co$. This difference reflects a modification of the phase relationship between the instantaneous orbital velocity and the resulting torque response. In the opposing configuration, the larger phase shift combined with the nearly degenerate ellipse indicates that the torque variations remain closely inherent to the velocity component, with limited contribution from acceleration-driven effects. Conversely, in the co-current case, the reduced phase lag together with the inertial effect reveals a strong balance between velocity and acceleration contributions. The torque response therefore reflects a persistent coupling between velocity modulation and inertial mechanisms, leading to a modulated dynamic behaviour depending on the wave case considered.

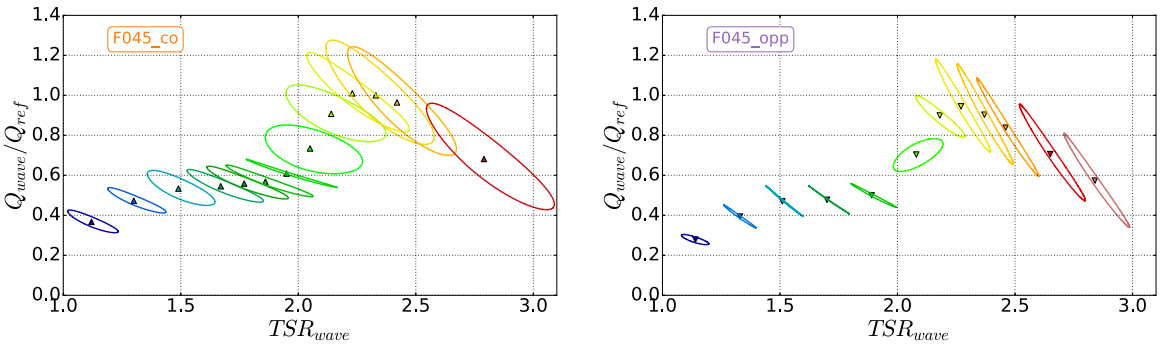
The extended Morison-type formulation reproduces this transition in behaviour, predicting both the persistence of coupled inertial effects in the co-current configuration and the collapse of the inertial contribution in the opposing case, when near-bed orbital velocities become small relative to the mean flow (approximately 5% in the present configuration). This capability to account for wave–current incidence effects is essential for applying the model under realistic sea-state conditions.

3.3. Model application on irregular sea states

Although monochromatic wave conditions provide a necessary framework for identifying the physical mechanisms and calibrating the hydrodynamic coefficients of the model, the predictive capability of the formulation must be assessed beyond the calibration cases. For these tests, the wave-induced torque fluctuations are primarily driven by the wave orbital velocity experienced by the turbine. Although the imposed wave frequency remains well defined, the finite variability of the wave amplitude observed experimentally results in a corresponding modulation of the orbital velocity amplitude. This modulation is consequently reflected in the amplitude of the wave-induced torque fluctuations, which do not necessarily exhibit a constant-amplitude behaviour. The present section therefore evaluates the robustness of the proposed Morison-type approach in two successive steps. First, the model is applied to reproduce torque fluctuations under monochromatic wave conditions at a given operating point, using a unique set of calibrated coefficients. Second, the same coefficients are employed under an irregular JONSWAP-type sea state in order to assess the capacity of the formulation to handle realistic multi-frequency inflow conditions.

To do so, the instantaneous inflow velocity used in the model is obtained from PIV measurements performed upstream from the rotor column, as presented in Appendix A. The measured streamwise velocity field is vertically averaged over the turbine height to obtain a representative local inflow velocity. The resulting velocity signal is then interpolated onto the temporal sampling of the torque measurement. The velocity and torque signals are subsequently temporally aligned using a cross-correlation procedure, which provides the optimal time lag between the local inflow fluctuation and the measured torque response. Fig. 31 presents the reconstruction of the temporal fluctuating torque signal $Q'_{wave}(t)$ for a monochromatic wave case ($F060_A1$, $U_0 = 0.8$ m/s) at $TSR \simeq 2.4$. The reconstruction is based on a single set of coefficients (C_{Q0}, C_{Q1}, C_{MQ}) identified under monochromatic wave conditions at the corresponding mean operating point.

The reconstructed signal reproduces the main features of the measured torque fluctuations, including their phase and amplitude modulation at the imposed wave frequency. The variations in oscillation amplitude observed in the experimental signal are consistent with the finite variability of the wave-induced orbital velocity, which follows the temporal evolution of the wave amplitude. The normalised standard deviation from the reconstruction (18%) remains close to the filtered experimental value (16%), with a coefficient of determination R^2 about 0.95. This result confirms that the readapted Morison formulation preserves the essential dynamic features of the turbine response when applied outside the direct identification dataset, provided that the mean operating point remains unchanged.



(a) $F045_co$ (b) $F045_opp$

Fig. 29. Phase distributions of the torque Q_{wave}/Q_{ref} as a function of TSR_{wave} for the two wave cases $F045_co$ and $F45_opp$ at $U_0 = 0.8$ m/s.

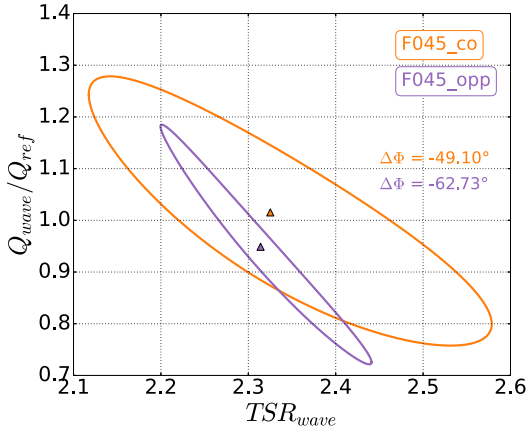


Fig. 30. Comparison of the torque distributions for the $F045_co$ and $F045_opp$ cases, TSR ≈ 2.3.

Table 6
Irregular wave case characteristics (JONSWAP-type) evaluated from the measurements carried out during the tests ($U_0 = 0.8$ m/s).

Wave case	Peak period T_p [s]	Wave height H_s [m]	γ
JS	1.67	0.09	3.33

Having validated the model under controlled wave conditions, its applicability to irregular sea states is now investigated. In realistic marine environments, tidal turbines operate under broadband wave spectra commonly described by JONSWAP or Pierson-Moskowitz formulations. The characteristics of the JONSWAP case considered here are summarised in Table 6. No additional calibration is performed. The coefficients used for the reconstruction are those identified for the regular wave case $F060_A1$, whose frequency coincides with the spectral peak of the JONSWAP condition ($f_p = 1/T_p$ which is about 0.60 Hz). Since the dominant contribution to the orbital velocity variance in a JONSWAP spectrum is concentrated around the peak frequency, this choice provides a dynamically representative set of hydrodynamic coefficients without introducing additional adjusted parameters.

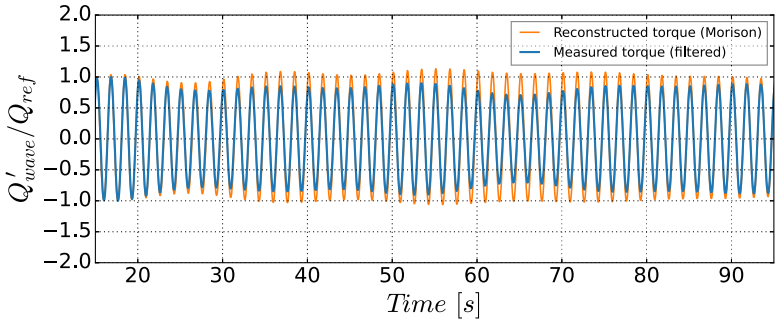
Fig. 32 then shows the reconstruction of the temporal torque fluctuations under this irregular loading. Despite the increased spectral complexity of the inflow, the main temporal modulations are correctly reproduced in both amplitude and distribution. The correlation level remains high ($R^2 = 0.91$) and the normalised standard deviation of the reconstructed signal (6.5%) closely matches the filtered experimental value (6.3%). These results indicate that the temporal superposition of wave components is consistently captured by the formulation, even though the coefficients were identified exclusively under monochromatic wave conditions. The residual discrepancies between measured and reconstructed signals can be attributed to several factors. The inflow velocity is measured upstream from the rotor column and does not account for local flow modifications induced by the turbine itself, nor for potential time lags between the measurement plane and the torque generation region. Additionally, the use of a single coefficient set associated with the mean operating point does not fully capture the instantaneous variations of TSR induced by simultaneous fluctuations of inflow velocity and rotational speed, although the latter remain limited ($\sigma(\omega) \leq 3\%$ of the imposed ω_0). In irregular sea states, further discrepancies may arise from the intrinsic distribution of wave amplitudes and frequencies. Unlike the monochromatic-wave case, where a single orbital amplitude governs the response, the JONSWAP condition involves a stochastic superposition of components with varying amplitudes.

Overall, the proposed Morison-type model demonstrates a robust predictive capability across both monochromatic and irregular wave conditions using a limited number of calibrated parameters. The results support the interpretation of wave-induced effects as a perturbation around a mean operating point, whose intensity is primarily governed by the local orbital ratio. From a practical perspective, the use of conservative or envelope coefficients identified under wave loading appears as a promising strategy to bound torque fluctuations under realistic sea states. Such an approach would provide a compact and operational modelling framework, positioned between purely linear spectral transfer-function methods and computationally intensive fully unsteady numerical models.

4. Conclusion

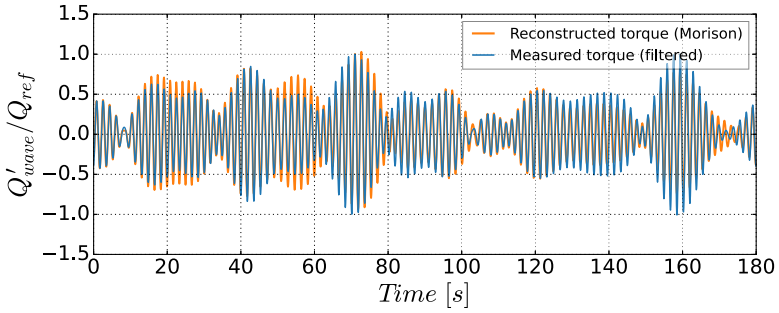
This work provides an experimental investigation of the behaviour of a vertical axis tidal turbine subjected to combined wave–current interaction, representative of conditions expected at the real scale turbines deployment site (Alderney Race). A detailed analysis of the turbine torque response under monochromatic waves is carried out through experimental testing at a 1:20 scale. The study emphasises the effects of wave parameters on the wave-related turbine response: amplitude, frequency and incidence relative to the incoming flow.

The results show that, for the tested operating conditions, the mean power production and mean torque levels remain only weakly affected by wave propagation. The global operating regimes therefore remain comparable to those observed under current-only conditions. However, waves induce significant fluctuations around these mean values, reaching up to approximately 30% depending on the operating point and wave parameters. While the average operating state is preserved, waves generates marked excursions around the nominal TSR,



Q'_{wave}	$\sigma(Q_{wave})/Q_{ref}$ [%]
Filtered	16
Reconstructed	18
R^2	0.95

Fig. 31. Reconstruction of the normalised torque temporal fluctuations for the $F060_A1$ case and $U_0 = 0.8$ m/s. The TSR studied is $TSR = 2.4$. PIV measurements are carried out upstream from the rotor column (Appendix A).



Q'_{wave}	$\sigma(Q_{wave})/Q_{ref}$ [%]
Filtered	6.3
Reconstructed	6.5
R^2	0.91

Fig. 32. Reconstruction of the torque temporal fluctuations for an irregular wave case (JONSWAP) and $U_0 = 0.8$ m/s. The TSR studied is $TSR = 2.4$. PIV measurements are carried out upstream from the rotor column.

potentially favouring repeated local transitions between neighbouring regimes. Spectral and phase-averaged analyses demonstrate that the wave-induced torque component strongly depends on the operating regime. The relative contribution of wave loading varies with the local slope of the stationary $C_Q(TSR)$ curve and with the orbital velocity ratio at the turbine height. These observations underline that the turbine response to waves cannot be solely reduced to a proportional relationship between wave action and mechanical output. Instead, the dynamic response is intrinsically related to the instantaneous operating point.

In this context, a Morison-like formulation extended to the turbine torque is proved to effectively reproduce the wave-related torque behaviour. It provides physically interpretable terms and coefficients associated to velocity-related and inertia-related (orbital acceleration) mechanisms. The introduction of a limited set of empirical coefficients (C_{Q0}, C_{Q1} and C_{MQ}) provides a consistent framework to describe the influence of waves across operating regimes. The coefficient C_{Q0} characterises the evolution of the mean torque level, C_{Q1} governs the local dynamic behaviour around the operating point revealing amplification or damping of TSR fluctuations, while C_{MQ} quantifies the inertial contribution associated with orbital acceleration. The formulation shows that the ratio between orbital and incoming flow velocity at the turbine location is a key indicator for predicting the level of wave-induced torque fluctuations around the mean torque. A phase-averaged analysis reveals that the torque response is related to a characteristic elliptical distribution when displayed in the $(TSR_{\text{wave}}, Q_{\text{wave}})$ space. This formulation establishes a direct connection between wave-induced torque dynamics and the classical stationary torque-TSR representation. In particular, it enables identification of operating regimes for which wave-induced TSR fluctuations are either amplified or attenuated in the torque response, offering a stability-oriented interpretation of wave-turbine interaction.

Wave parameters modulate these components with their own specificities. Increasing wave height primarily increases the velocity-related component (up to 20% between the wave cases here), while increasing wave frequency also alters the inertial response. These variations are largely attributed to changes in the orbital ratio. Furthermore, the opposition of the wave direction to the current reduces the orbital

penetration for the lower part of the water column. It consequently weakens the inertial contribution compared to the case of waves following the current. These effects persist across flow velocity regimes, although the relative magnitude of fluctuations increases when the mean flow decreases, due to the larger local orbital velocity ratio. The extension of the analysis to irregular sea states demonstrates that the identified coefficient set remains sufficient to reproduce the transient torque response. This confirms the robustness of the reduced-order formulation beyond monochromatic wave conditions.

Overall, this study demonstrates that phase-averaged characterisation and extended Morison modelling offer an effective methodology to quantify and analyse wave-induced effects on vertical axis tidal turbines. Beyond the specific geometry tested in this work, the proposed modelling has a broader relevance for vertical axis technologies. Because the formulation directly captures the mechanisms governing wave–current interaction, it can be transposed to different VATT architectures and operating regimes. This emphasises the potential of the model as a generic tool for predicting wave-induced torque fluctuations and for supporting design optimisation or control strategies across vertical axis technologies, based on the perspective of describing the wave-related torque sensitivity to disturbances (Shapiro et al., 2021). From an operational perspective, torque fluctuations directly affect power output. Wave-induced torque modulations therefore translate into short-term power variability, a key aspect for grid integration and power smoothing strategies. Reliable prediction of these fluctuations is thus essential for both performance assessment and stable network operation. Beyond power and torque considerations, the same formulation can be extended to estimate wave-induced hydrodynamic load fluctuations on rotating structures. By providing a compact description of cyclic load amplitudes, the model constitutes a practical tool for structural dimensioning and fatigue analysis under realistic sea-state conditions. The proposed Morison-like framework enables hydrodynamic modelling, control-oriented prediction and structural assessment, offering an applicable engineering approach for vertical axis tidal technologies.

CRediT authorship contribution statement

Y. Saouli: Writing – original draft, Visualization, Methodology, Investigation, Formal analysis, Conceptualization. **B. Gaurier:** Writing – review & editing, Validation, Investigation, Formal analysis. **G. Germain:** Writing – review & editing, Supervision, Project administration, Conceptualization. **G. Maurice:** Writing – review & editing, Resources, Project administration.

Declaration of competing interest

The authors declare that they have no known competing financial interests or personal relationships that could have appeared to influence the work reported in this paper.

Acknowledgements

This work received the financial support of the French Agence Nationale de la Recherche through the Verti-Lab project (ANR-23-LCV1-0009-01), the French Research and Technology National Association (ANRT) under the convention Cifre n° 2023/0217 and the CPER IDEAL. The authors acknowledge Jean-Valéry Facq and Cédric Derveaux for the model design, as well as Christophe Penisson and Benoit Gomez for their help during the tests and the data analysis.

Appendix A. Experimental validation

In addition to the theoretical approach based on the presented wave theory, Particle Image Velocimetry (PIV) measurements are also performed to assess the actual orbital velocity profiles upstream from the turbine. The measurements are made using Hisense Zyla 5.5M pixel cameras, with 16-bit greyscale depth per pixel. The acquisition is carried out at a sampling frequency of $f_s = 15$ Hz, for a duration of 120 s. The vertical PIV planes are extended on 0.60 m longitudinally and cover the turbine height. The spatial resolution in both streamwise and vertical directions is $dx = dz = 0.01$ m.

Fig. 33 displays the velocity profiles at three positions in the plane. The differences emphasise the inductive effect of the turbine, with a decrease of 7% of the mean velocity profiles from $x = -0.6$ m to $x = -0.4$ m. Furthermore, the influence of wave action is observable through the standard deviation of the velocity profiles. The fluctuations become increasingly significant as the surface is approached, reflecting the depth-dependent evolution of wave orbital velocities. This trend underscores the non-uniform distribution of wave energy along the depth, with stronger orbital velocities near the free surface.

These measurements allow for a direct comparison between the theoretical predictions and the experimentally observed velocity fields.

Fig. 34 shows the experimental/theoretical comparison for three wave cases, considering the three levels of u_w/U_0 previously observed. The orbital velocity is deduced from the experimental measurements by applying a narrow band-pass filter around the average wave frequency [f_{wave} - 0.05 ; f_{wave} + 0.05]. The orbital velocity profile can then be captured from the measurements for the turbine height. The results obtained over the tested wave conditions show good agreement between the measured and theoretical profiles in terms of velocity amplitude and vertical distribution, the differences between experimental and theoretical profiles falling within the measurement uncertainty associated with PIV measurement (about 6 to 8% from the GUM method, as developed by Ikhennicheu (2019)). This consistency, together with the low KC values (< 0.2), supports the use of the theoretical velocity profiles in the remainder of the study as a reliable and systematic representation of the wave-induced flow.

Appendix B. Torque coefficient evolution, $U_0 = 0.6$ m/s

Fig. 35 presents the evolution of the phase-averaged torque coefficient $\overline{C_Q}$, normalised by the reference maximum torque coefficient $C_{Q,ref}$, as a function of the TSR.

At the flow velocity $U_0 = 0.6$ m/s, the observed trends remain globally consistent with those obtained for $U_0 = 0.8$ m/s, although the relative wave effects become even more pronounced. Fluctuation intensities reach up to 50% over the range of tested TSRs, with comparable levels observed for the different wave conditions. Compared with the reference current-only case, this corresponds to a variability up to twice as large for $TSR \geq 2.3$.

It should also be noted that the relative variations of the mean coefficients observed for $TSR \leq 2.0$ at $U_0 = 0.6$ m/s are attributed to Reynolds number effects associated with the critical turbulent regime encountered in these conditions. Similar mean coefficients with and without waves are however recovered for the higher velocity cases $U_0 = 0.8$ m/s.

Appendix C. Wave-related torque evolution, F060_A1, $U_0 = 0.6$ m/s

Fig. 36 displays the wave-related torque distribution in the space of representation (TSR_{wave}, Q_{wave}) at $U_0 = 0.6$ m/s. The elliptical shape of the wave-related torque is found for the four wave cases and corroborate the difference in the ellipses dimensions and orientation. Compared to the $U_0 = 0.8$ m/s, the wave-related fluctuations around the average torque are more important as the normalised Q_{ref} at $U_0 = 0.6$ m/s is smaller. The orbital ratio u_w/U_0 is also found to be greater in these cases.

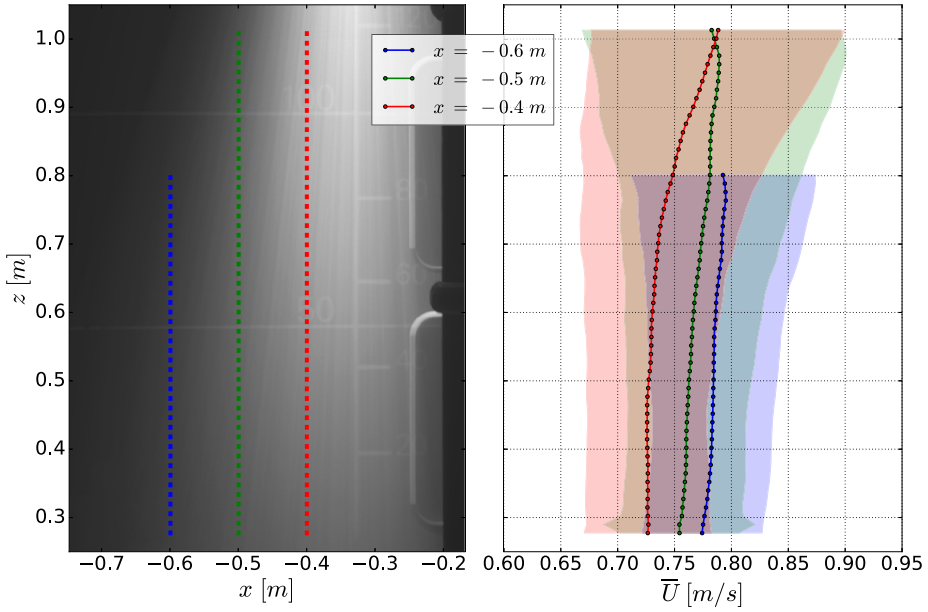
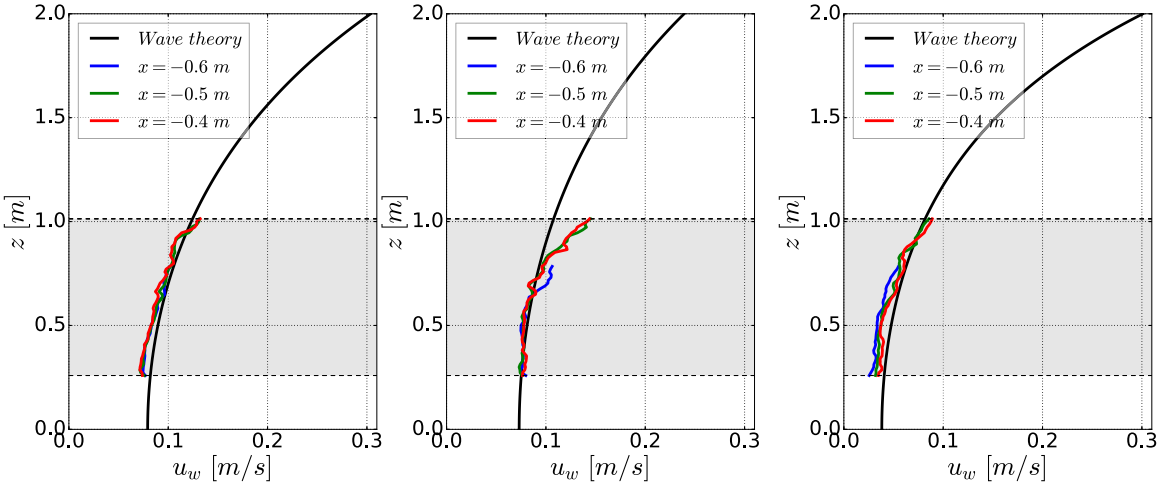


Fig. 33. PIV plane upstream from the turbine for the *F*060_*A*2 case. The orbital velocity profiles are extracted from the three dotted lines positions presented in the plane.



(a) *F*060_*A*2, $U_0 = 0.6$ m/s **(b)** *F*060_*A*2, $U_0 = 0.8$ m/s **(c)** *F*045_*opp*, $U_0 = 0.8$ m/s

Fig. 34. Experimental velocity u_w profiles (PIV) in comparison with the Airy wave theory. The comparison is done for three cases with different u_w/U_0 ratios. (a) F060_A2 at $U_0 = 0.6$ m/s. (b) F060_A2 at $U_0 = 0.8$ m/s. (c) F045_opp at $U_0 = 0.8$ m/s.

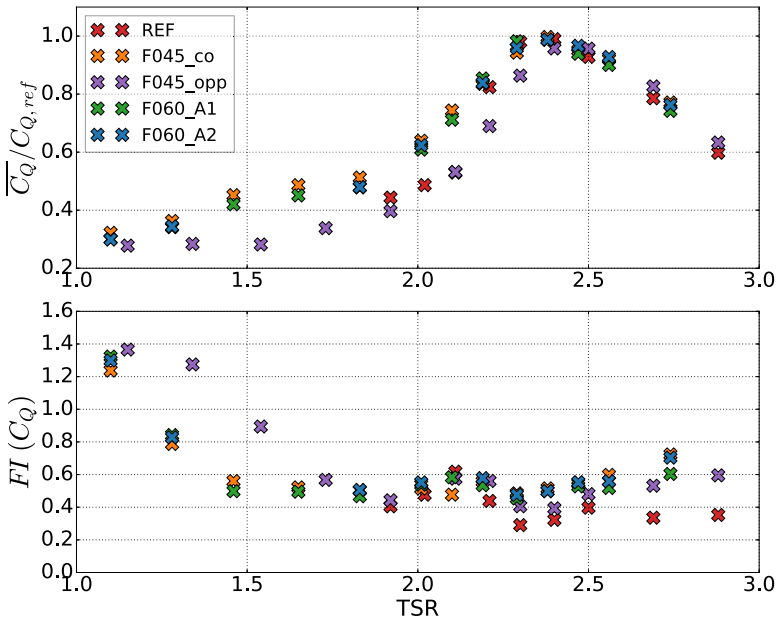
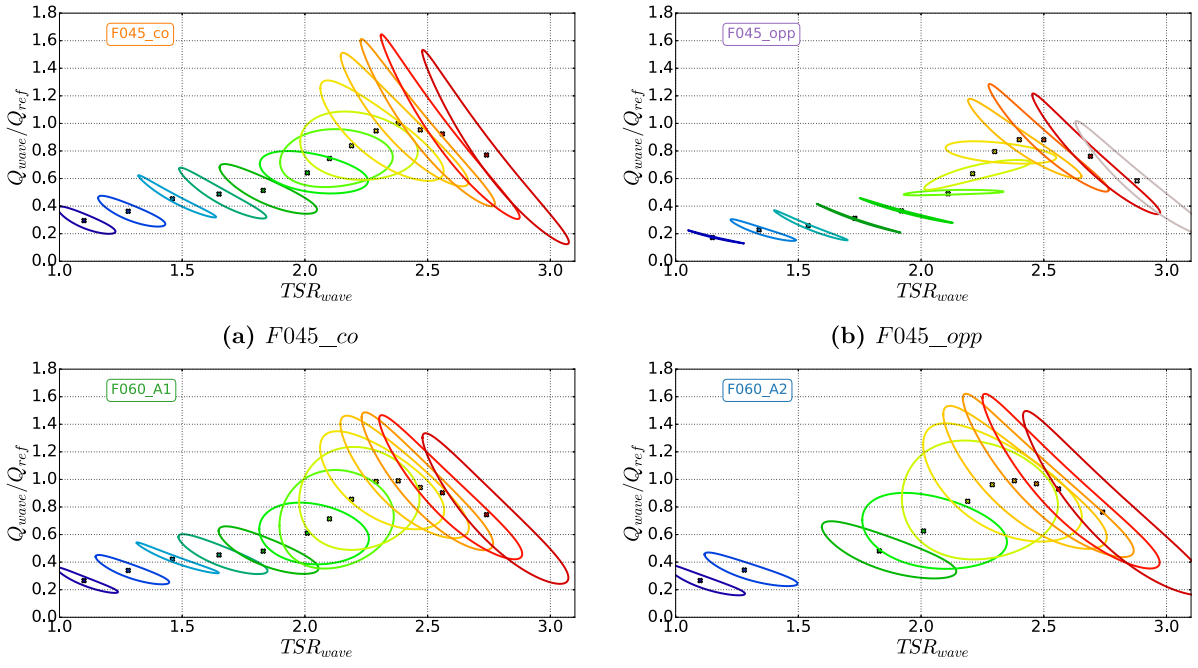


Fig. 35. $\overline{C_Q}/C_{Q,ref}$ and the FI(C_Q) curves for the reference case (no wave) and the four wave cases tested. $C_{Q,ref}$ is defined as the maximum torque coefficient obtained without waves for the flow velocity $U_0 = 0.6$ m/s.



(a) $F045_co$ (b) $F045_opp$

(c) $F060_A1$ (d) $F060_A2$

Fig. 36. Evolution of the wave-related torque formulations depending on the wave-related TSR for the wave cases at $U_0 = 0.6$ m/s.

References

Allmark, M., et al., 2021. A phenomenological study of lab-scale tidal turbine loading under combined irregular wave and shear flow conditions. J. Mar. Sci. Eng. 9 (6).

Arcos, F., et al., 2025. Tidal turbines under combined currents and waves: experimental and numerical study. Proc. Eur. Wave Tidal Energy Conf. 16.

Bai, J., et al., 2025. Dynamic response of the jacket offshore wind turbines subjected to coupled wind, wave, and earthquake loads under scour conditions. Ocean Eng. 328, 120901.

Bossard, J., 2012. Experimental Caracteristics of dynamic stall in HARVEST Turbines with Particles Image Velocimetry method (PIV). Comparing with modeling results (Ph.D. thesis). (2012GRENI034), University of Grenoble.

Bureau Veritas, 2015a. Guidance note NI 603 – current and tidal turbines. URL https://marine-offshore.bureauveritas.com.

Bureau Veritas, 2015b. Hydrodynamics technical bulletin – application of morison-type formulations. Internal technical communication, available on request.

Chawla, A., et al., 2021. Wave modeling in coastal and offshore applications. Annu. Rev. Fluid Mech. 53, 441–469.

Dean, R.G., et al., 1991. Water Wave Mechanics for Engineers and Scientists. WORLD SCIENTIFIC.

Druault, P., et al., 2026. POD analysis of regular waves interacting with large scale flow structures in the water column. Ocean Eng. 352, 124601.

Dufour, M., et al., 2026. Experimental and analytical study of surface waves effects on a horizontal axis tidal turbine: loads and wake dynamics investigation. J. Ocean. Eng. Mar. Energy.

Fu, L., et al., 2021. Numerical modelling of wave–current interactions on a tidal turbine using openfoam. Renew. Energy 170, 1–14.

Gaurier, B., et al., 2020. MaRINET2 tidal energy round robin tests—Performance comparison of a horizontal axis turbine subjected to combined wave and current conditions. J. Mar. Sci. Eng. 8 (6).

Gaurier, B., et al., 2025. Wave effects on large scale turbulent flow structures propagating in the water column. Mar. Energy Res..

Guillou, S., et al., 2021. Wave–current interactions and their impact on tidal energy resource assessment: Application to the alderney race (raz blanchard). Energies 14 (12), 3625, (Accessed May 2025).

Guo, X., et al., 2018. The surface wave effects on the performance and the loading of a tidal turbine. Ocean Eng. 156, 120–134.

Henriques, R.d., et al., 2022. A morison-based model to predict unsteady hydrodynamic loads on tidal turbines under combined wave and current conditions. Renew. Energy 201, 577–592.

Huang, R., et al., 2024. Research on bidirectional fluid-structure interaction characteristics of horizontal axis tidal turbines under wave current conditions. Ocean Eng. 294, 116806.

Húsgard, J., et al., 2020. OMA-based modal identification and response estimation of a monopile model subjected to wave load. In: Topics in Modal Analysis and Testing, Volume 8. Springer International Publishing, pp. 237–245.

IEC, 2013. Marine energy - wave, tidal and other water current converters - part 200: Electricity producing tidal energy converters - power performance assessment.

Ikhennicheu, M., 2019. Experimental study of the turbulence in high flow velocity areas and its impact on tidal turbines (Ph.D. thesis).

Ikhennicheu, M., et al., 2019. In: B.V., E. (Ed.), Experimental study of coherent flow structures past a wall-mounted square cylinder. 182, pp. 137–146, Article. FRANCE..

Jaquier, T., 2011. Cross-flow Water Turbines: Development of a HARVEST Prototype in Water Channel (Ph.D. thesis). (2011GRENI059), University of Grenoble.

Konstantinidis, E., et al., 2017. Drag and inertia coefficients for a circular cylinder in steady plus low-amplitude oscillatory flows. Appl. Ocean Res. 65, 219–228.

L. Furgerot, A.S., 2020. One year of measurements in alderney race: preliminary results from database analysis. Philos. Trans. R. Soc. A: Math. Phys. Eng. Sci..

Linant, R., et al., 2025. Experimental study of the wave effects on a ducted twin vertical axis tidal turbine wake development. J. Mar. Sci. Eng. 13 (2).

Mackay, E.B.L., et al., 2022. Joint extremes of waves and currents at tidal energy sites in the english channel. In: International Conference on Offshore Mechanics and Arctic Engineering, Volume 8: Ocean Renewable Energy.

Martinez, R., et al., 2021. Tidal energy round robin tests: A comparison of flow measurements and turbine loading. J. Mar. Sci. Eng. 9 (4).

Marty, A., et al., 2022. Experimental study of two kinds of hard marine growth effects on the hydrodynamic behavior of a cylinder submitted to wave and current loading. Ocean Eng. 263, 112194.

McNaughton, J., et al., 2025. Dynamic loading of two side-by-side tidal stream turbines in regular waves. J. Fluids Struct. 133, 104259.

Moreau, M., et al., 2023a. Experimental investigation of surface waves effect on a ducted twin vertical axis tidal turbine. J. Mar. Sci. Eng. 11 (10).

Moreau, M., et al., 2023b. Experimental performance and wake study of a ducted twin vertical axis turbine in ebb and flood tide currents at a 1/20th scale. Renew. Energy 214, 318–333.

Morison, J.R., et al., 1950. The force exerted by surface waves on piles. Pet. Trans. Am. Inst. Min. Eng. 189, 149–154.

Nachtane, M., et al., 2020. A review on the technologies, design considerations and numerical models of tidal current turbines. Renew. Energy 157, 1274–1288.

Phillips, M., 1967. The dynamics of the upper ocean. By 0. m. PHILLIPS. Cambridge uni-versity press, 1966. 261 pp. 60s.. J. Fluid Mech. 29 (4), 822–825.

Saouli, Y., et al., 2025. Experimental investigation of the flow direction effects on a quadrirotor vertical axis tidal turbine. Ocean Eng. 341, 122519.

Schmitt, P., et al., 2016. Hydrodynamic loads on tidal stream turbine blades: Comparison between CFD and BEMT. In: Proceedings of the 4th International Conference on Renewable Energies Offshore. RENEW, Lisbon, Portugal.

Shapiro, C., et al., 2021. Hydrokinetic turbine control for maximizing power capture in unsteady flow conditions. Renew. Energy 164, 703–714.

Thiébaut, M., et al., 2018. Monitoring tidal currents with a towed ADCP at tidal energy site in Alderney Race (Raz Blanchard). In: Soares, C.G. (Ed.), Advances in Renewable Energies Offshore Proceedings of the 3rd International Conference on Renewable Energies Offshore (RENEW 2018), October 8-10, 2018, Lisbon, Portugal. Taylor & Francis, Lisbonne, Spain, pp. 49–56.

Vicinanza, D., et al., 2019. Wave energy resource assessment and its potential for the mediterranean sea. Renew. Energy 135.

Wang, L., et al., 2021. Wave–current effects on tidal stream turbine performance and wake characteristics. Renew. Energy 172, 479–493.

Wang, S., et al., 2026. CFD-machine learning integrated global sensitivity analysis of horizontal axis tidal turbine under wave-current loading. Renew. Energy 262, 125430.

Yamada, S., et al., 2016. Effect of the Reynolds number on the performance and approximate modeling of the small straight-bladed vertical-axis wind turbine. J. Fluid Sci. Technol. 11, JFST0014–JFST0014.

Zanforlin, S., et al., 2020. Effect of waves on tidal turbine performance and wake characteristics. Renew. Energy.